Analyzing internal shearing in compound landslides using MPM

Nahmed Nissar

Thesis submitted to the faculty of the Virginia Polytechnic Institute and State University
in partial fulfillment of the requirements for the degree of

Master of Science
In
Civil Engineering

Alba Yerro-Colom, Chair
Adrian Rodriguez-Marek
Joseph Dove

June 15, 2020
Blacksburg, VA

Keywords: Compound landslides; Material Point Method; Internal shearing; Barriers

Analyzing internal shearing in compound landslides using MPM

Nahmed Nissar

ABSTRACT (academic)

Landslides cause significant damage worldwide and therefore epitomize the most important problems in geotechnical engineering. Hence, perceiving the mechanics involved in the deformation process of landslides is necessary for risk assessment. In addition to the resistance offered by basal shear surfaces, internal shearing also influences the stability and kinematics of compound landslides. For compound landslides, internal shearing is essential to develop feasible sliding mechanisms. The internal distortion is caused by the formation of shear bands that develop within the sliding mass. The strain localization is generally attributed to slope changes along the basal sliding surface (or topography) that constrain the strain field of the landslide. The development of these internal shear bands also controls the energy dissipation, and its distribution determines the final degradation of the material. This work focuses on the study of internal failure mechanisms that develop in compound landslides. A theoretical model of a compound landslide is numerically analyzed using the Material Point Method (MPM), a state-of-the-art numerical technique appropriate to model large deformation problems. The internal failure pattern is identified for different basal sliding geometries. Based on that, a generalized method is proposed to estimate the internal failure mechanism of bi-planar compound geometries. The material degradation and energy dissipation are evaluated in terms of the accumulated deviatoric strain and the reaction forces exerted by the landslide on a vertical wall. Moreover, preliminary studies are conducted to analyze the use of barriers as a mitigation strategy to counter landslide damage, and their efficiencies are investigated.

Analyzing internal shearing in compound landslides using MPM

Nahmed Nissar

ABSTRACT (general audience)

Landslides consist of movement of rock and debris down a slope. They cause substantial damage each year and therefore represent an important class of problems in geotechnical engineering. Understanding the deformation process and internal shearing pattern occurring in landslides is an important aspect for assessing the risk that a landslide poses. The internal shear is caused due to the formation of shear bands that develop within the mass flowing down the slope and originate at the points of slope change on an incline. These shear bands also affect the amount of energy dissipated and the degradation of flow material. In this work, the internal failure mechanism in landslides is analyzed and effects on landslide kinematics are studied. Material Point Method (MPM) is used to simulate slope instabilities which is an advanced numerical technique appropriate for modeling large deformation problems such as landslides. Several theoretical models of compound landslides are presented considering variation in geometry (roundedness), friction, and slope angle. A generalized failure mechanism of a landslide is proposed based on its geometry and physical parameters. Finally, accumulated strains and reaction forces impacted by moving mass on a wall are calculated for different landslide geometries, and subsequently correlated to energy dissipation material degradation. These results also serve as a precursor to studying the role of barriers in mitigating landslide damage.

ACKNOWLEDGMENTS

Foremost, I would like to thank Almighty for blessing me with the strength and aptitude to conduct research and complete this work during challenging times of COVID-19.

I am deeply indebted to Dr. Alba Yerro-Colom for being an excellent research advisor, and for her constant support during my master's course at Virginia Tech. I am immensely thankful for her patience, motivation, enthusiasm, and expertise in the subject. Her valuable feedback and guidance provided the right direction for my research, and drafting of this thesis. I could not have imagined having a better guide for my master's thesis project.

I thank the rest of my thesis committee: Prof. Adrian Rodriguez-Marek, and Dr. Joseph Dove for their encouragement and helpful suggestions. I also appreciate the contribution of Dr. Alba's research group, especially Luis Eduardo Zambrano, for always being there to answer my questions and helping me work out software issues that I encountered frequently.

My sincere gratitude goes to Mr. Rajul Teredesai and Dr. Zarghaam Rizvi for providing internship opportunities at graduate and undergraduate levels, respectively, and supervising my work on diverse projects.

I am grateful to my colleagues at Virginia Tech: Yusheng Jiang, Samuel Consolvo, Dennis Kiptoo, and my flat mate Vikas Gurram for their vital support. Special thanks to my friends Syed Azhar Ali, Akhil A. Rafeeq, and Parthkumar Modi for all the fun times in Blacksburg.

Finally, I would like to show appreciation my friends and family in India, especially my parents and grandmother, for nurturing and supporting me emotionally throughout my life.

Table of Contents

List of Tables

List of Figures

1 Introduction

1.1 Background and motivation

Landslides are natural disasters and cause enormous damage to humankind and property every year. Roughly 25-50 people lose their lives annually in the United States because of landslides (USGS 2020). As far as the worldwide death toll is concerned, thousands die each year due to landslides. Primarily, these casualties result from rock falls, debris-flows, flow slides, and volcanic debris flow (known as lahars). More than 2,600 fatal landslides recorded between 2004 and 2010 resulted in more than 32,000 casualties (Petley 2012).

Therefore, it is imperative to understand the mechanics involved in the mass flow of a landslide on a large scale. While the stability and kinematics of a slope depend mostly on the resistance of the basal slip surface, the internal distortion and degradation of the material can also influence the kinematics, especially in compound landslides. Compound landslides consists of an active block which drives a more stable passive block (Hungr et al. 2014). These are different from translational slides where the entire body slides in an active state. Due to complex motion in more than one direction, internal shearing affects the kinematics of compound landslides.

Taking these facts into account, it can be stated that examining the damage caused by compound landslides is essential. Moreover, to keep people and buildings safe from such damage, the following questions need to be addressed to:

- How does internal shearing occur in a landslide? How does internal shearing impact the kinematics of compound landslides? What methods have been used to study internal shearing patterns in a compound landslide?
- Given a landslide geometry, can we predict failure patterns around slope transitions following a generalized mechanism?
- Can we correlate the failure geometry with the material shearing and degradation? Further, can we estimate corresponding energy losses occurring at slope transitions in compound landslides?

- How can we mitigate the damage caused by compound landslides? Can we design some barriers that could effectively reduce the velocity of moving particles in a landslide? If so, what could be a possible efficient design?

These are some of the key questions that need to be addressed. To search for answers, we need to make use of numerical tools and techniques that can accurately model the post-failure behavior of a compound landslide. The numerical modeling of these processes is challenging because of the large deformations suffered by the material during the motion. So, understanding the mechanisms involved in the whole deformation process is of utmost importance for risk assessment.

The Material Point Method (MPM) is considered as one of the most suitable methods to model this type of geotechnical problems due to its capability to handle large deformation problems (Soga et al., 2016). Especially in geotechnical engineering problems such as landslides, MPM has been shown to successfully capture the post-failure behavior of a landslide and predict the runout, velocity, and displacement of soils with high accuracy. Owing to these attributes, MPM can potentially emerge as a useful numerical tool to analyze the failure mechanics and risk associated with compound landslides.

1.2 Research goals and plan

The goals of this research are to:

- Analyze various types of geometries of compound landslides using MPM and observe internal shearing patterns.
- Propose a generalized internal failure mechanism detailing shear band formation and strain localization, given a known landslide geometry (slope, radius of curvature of the slope transition), strength parameters at the basal sliding surface, and material properties.
- Examine the effects of internal shearing on landslide kinematics, and qualitatively correlate failure geometry landslide with material degradation.

- Qualitatively study the energy dissipation occurring at slope transitions in compound landslides through analyzing the impact of the mobilized mass against a rigid vertical structure.
- Investigate the role of protective barriers as a mitigation strategy to counter the damaging effects of a landslide.

To achieve these objectives, the research work performed in this thesis was organized in several tasks briefly described below:

First, we survey the academic literature on numerical methods employed to solve large deformation problems, and analyze the merits and demerits of each technique. We then point out some of the previous work done on the causes and consequences of compound landslides.

Subsequently, we propose a theoretical model of a compound landslide. We modeled the slope using MPM along with Anura3D software to identify the internal shear pattern in different compound landslides. This is accomplished by performing a parametric analysis varying the slope angle, the radius of curvature of slope transition, the basal friction coefficient, and the length of the basal shear surface.

Then, we identify the regions of strain localization, or shear bands by assessing the regions of maximum incremental deviatoric strain by post-processing the numerical results. Further, to evaluate material degradation caused due to internal shearing, we compute and compare the cumulative deviatoric strain among numerous basal geometries. Then, we correlate the failure geometry with the material degradation.

The energy dissipation is qualitatively estimated by studying the impact forces on a vertical structure (i.e., rigid wall) located at the end of a landslide runout. We determine the magnitude of the reaction force impacted by the landslide on their collision with the vertical wall at the end of the basal sliding surface. These reaction forces provide a good idea about kinetic energy losses due to changes in internal shearing occurring in slope transitions.

Finally, we conduct some preliminary simulations involving multiple protective barriers to gain elementary insights into mitigation strategies countering landslide damage. These models involve soil placed at the top of an incline that slides under gravity and gets

impacted by the barriers at regular intervals along the runout. We draw a relation between the number and height of the intermediate protective barriers, and the reduction in the reaction force on the final rigid wall.

1.3 Overview and organization of the thesis

This thesis is organized into four chapters.

- The first chapter corresponds to the introduction, which discusses the relevance of this research and presents the motivation, goals, and organization of the thesis. It also includes a literature review.
- The second chapter is an introduction and brief history of the Material Point Method (MPM). It also contains a validation section, where a laboratory experiment of a slope instability is reproduced with an MPM model.
- The third chapter contains most of the research performed in this thesis, which includes a description of the numerical model, the parametric analysis, and the discussion of the results. In particular, it proposes a generalized internal shearing mechanism for compound landslides, a qualitative study of energy dissipation, and the role of protective barriers as a mitigation strategy.
- The fourth chapter provides the thesis conclusions including a summary of the work conducted, the key findings, and recommendations for future work.

1.4 Literature review

A landslide is described as the movement of a rock or soil mass down a slope. Landslides have caused damage worldwide, including many places in the US. Previous research has mostly focused on the pre-failure behavior of landslides. This literature survey summarizes the conventional and state-of-the-art numerical techniques to solve large deformation problems in geotechnical engineering including landslides, discusses key contributions attempted at studying internal shearing in landslides and concludes that further research is essential to understand post-behavior of landslides on its kinematics, which in turn, is crucial for assessing risk and developing mitigation strategies.

Numerical techniques are nowadays being utilized as primary tools in almost all fields of engineering – mechanical, aerospace, material, and civil engineering, including geotechnical engineering. This shift from analytical to numerical techniques has happened because many problems are too complicated to be solved manually and to reduce the time and costs involved in conducting large-scale physical experiments. Computer simulations are also particularly useful when physical modeling is challenging and impossible to perform, as in the case of landslides, that are difficult to model owing to their large runouts and complex internal shearing mechanics.

At present, the Finite Element Method (FEM), developed in 1943 (Courant 1943), is the most popular numerical technique used to perform computer simulations. While FEM is recognized in both academic and industrial settings, this method reached its limits when the problem in consideration involves a substantial deformation – as in the case of a landslide where particles could travel a distance on the scale of kilometers. Hence, for large-deformation problems, FEM loses accuracy due to mesh distortion, which can cause the simulation to crash beforehand. While remeshing could be done, it is tough to derive an optimal mesh adaptation strategy.

To overcome these limitations from conventional numerical techniques, mesh-less and mesh-free methods started developing. In these approaches, the domain is discretized into various points (material-points) or particles, and each point interacts flexibly with its neighboring points while carrying the material properties, strain and stress. Some mesh-free techniques include: Smoothed Particle Hydrodynamics (SPH) by Gingold and Monaghan (1977), Generalized Finite Difference Method (GFDM) by Liszka and Orkisz (1980), and Material Point Method (MPM) by (Sulsky et al. 1994) were developed. This was followed by the Particle Finite Element Method (PFEM) of Idelsohn et al. (2006) and Sabel et al. (2014), and the Optimal Transport Meshfree method (OTM) by Li et al. (2010).

Recently, MPM has received a good deal of attention in geotechnical engineering, in particular, MPM was included in the 2017 Rankine Lecture. Fern et al. (2019) describe the use of MPM for many geotechnical problems. Soga et al. (2016) emphasize the need to develop numerical modeling methods that can predict both the failure initiation as well as the post-failure behavior of landslides. The authors discuss the merits and limitations of

various numerical techniques for modeling large-deformation problems involving landslides (including FEM, FDM, CEL, EFG, FEMLIP, SPH, PIC, and MPM), and finally suggest MPM overall. They also emphasize that MPM has the advantage of utilizing history-dependent constitutive models. Many recent publications in MPM have focused on landslides (Alonso 2014, Yerro 2016). Alonso et al. (2014) discussed the effect of rainfall on slope stability and presented the capabilities of modern Lagrangian methods like MPM to deal with large displacements. Yerro et al. (2016) studied the run-out of landslides in brittle soils, in which a saturated slope was analyzed. This work discusses both the pre-failure and post-failure behavior characteristics, such as run-out distance and sliding velocity, determined by employing the Mohr-Coulomb model with strain-softening behavior. The authors conclude that the initiation of progressive failure is controlled by peak strength whereas run-out is influenced by the residual strength of a material. The stability and kinematics of a landslide are governed by internal shearing apart from basal friction resistance.

Hungr (2014) describes compound landslides consisting of an active block which drives a more stable passive block, with complex motion in multiple directions. For compound landslides, Fell et al. (2007) considered internal shearing to be one of the most critical factors to understand rupture mechanisms in landslides, especially in rock and brittle materials. Hutchinson (1987) proposed that brittle internal shearing in compound landslides, buckling at toes, and sudden ingression of water into landslide mass could induce rapid sliding.

Fell et al. (2007) state that for compound slides, it is essential to determine if the nature of internal shearing is brittle since internal shearing is necessary to develop a feasible sliding mechanism. Rapid sliding is more likely in the case of brittle internal shear (strain weakening accompanied by small displacements on the internal shear surface). Brittle internal shears are expected if shear surfaces require fracturing of intact rock, more strength on internal shears than residual strength, and high Rock Quality Designation (RQD) of slide mass. Non-brittle internal shears are expected when if viable internal shear surfaces are parallel to existing continuous shear surfaces or bedding planes, internal shears are at residual strength and low RQD of slide mass.

Glastonbury and Fell (2010) studied 51 different landslides, in which they identified 26 to have been caused due to internal shearing. The typical volume of a landslide mass was of the order of 1 – 100 million cubic meters, with most of them occurring on slopes 20 – 40°. The authors observed that the internal shear band was generally perpendicular to main structures, or bedding planes, or at a high angle to anisotropy. The authors stated that passive wedges accounted for about 40% of the total slide volume, which implied significant load from the active wedge and internal shearing occurring at a high angle, approximately normal to the anisotropy.

Numerical research conducted on the mechanism of internal failure is limited. Yerro et al. (2016b) examine the stability conditions and the post-failure behavior of a compound deep-seated landslide, inspired in Vajont landslide. The authors analyze the internal shearing patterns and degradation using MPM for both pre-failure and post-failure conditions. Their results indicated that the stability of the compound slope is controlled by an internal shear band which develops along with a progressive failure mechanism.

The failure mechanism in a landslide, apart from controlling the failure initiation, also affects the kinematics, material degradation, and energy losses occurring during its motion. The design of protective barriers could also benefit from having a better understanding of internal shearing patterns, since they act like these sudden slope transitions. Physical barriers help to mitigate landslide damage and are employed in situations where landslides can potentially impinge on existing structures. Constructing buttresses, walls, barriers, and anchors at the base and regular intervals on the slope are some of the mitigation strategies for regions with a high probability of landslide incidents.

To mitigate landslide damage, further research needs to be conducted in the field of constructing protective barriers/obstacles to predict and reduce the velocity of the mass mobilized during a landslide. Dry granular materials tend to re-accelerate between consecutive rows of barriers placed on a slope due to gravity (Ng et al. 2018). Artificial barriers can alleviate the risk by lowering the velocity of particles and the final runout distance. They can also divert the flow towards lateral zones that are constrained by the barriers (Cuomo et al. 2019). Hence, protective barriers can prove to be effective in dissipating energy and alleviating damage.

Landslides continue to cause widespread damage throughout the world. For compound landslides, unfortunately, the research emphasizing internal shearing, strain localization, energy dissipation, using physical and numerical techniques has been sparse. Reflecting that immaturity, this literature survey defines the overall problem and points out gaps in understanding the failure mechanism of landslides, and its effects on landslide kinematics. Further research is needed to understand the internal shearing mechanism in landslides and predict failure patterns based on topography and material parameters to develop mitigation strategies for risk assessment.

2 The Material Point Method and validation with a physical experiment

2.1 The Material Point Method

2.1.1 A brief introduction to the Material Point Method

The Material Point Method was developed by Sulsky et al. (1994). It is one of the most recent developments of Particle in Cell Methods (PIC). The PIC technique dates back to 1950s by Harlow (1962) which was used to analyze fluid Mechanics problems at Los Alamos National Laboratory. However, the PIC methods suffered significant energy dissipation. Brackbill and Ruppel (1986) overcame this drawback using the FLIP (Fluid implicit particle method) technique. In 1994, Sulsky and her colleagues modified FLIP for applications in solid mechanics (Sulsky et al. 1994). Sulsky and Schreyer (1996) coined this new technique as Material Point Method (MPM) at the University of New Mexico.

In the Material Point Method, the continuum body is discretized by a predetermined number of Lagrangian particles or Material Points (MP). In addition to carrying external loads, these MPs carry all the information of the continuum such as mass, volume, density, gradient, displacement, velocity, acceleration, stress, strain, material parameters, strength parameters, etc. In geotechnical engineering problems, the MPs represent a small portion of the entire continuum and not the individual soil grains. Each material point moves attached with the solid body and hence constitutes the Lagrangian representation of the medium.

A Eulerian mesh is present which covers the entire domain in which the body is supposed to move. All displacements and deformations are numerically calculated in this computational mesh. The system of equilibrium equations is solved in the mesh grid, but usually it does not deform with the body, unlike FEM. Mapping functions are used to transfer the variables from the MPs to the nodes. The conservation of mass is satisfied because each material point contains a fixed amount of mass at all times.

2.1.2 The MPM algorithm

At the start of each time step, all the information regarding the material and state parameters (e.g., density, stress, strain, velocity, etc.) remain at the MPs. The MPM algorithm can be summarized as follows (Figure 2.1):

a) The material points (shown in black) are overlain on a computational mesh. The blue arrows represent material state parameters like velocity, mass, etc. These are projected towards the computational grid nodes by using shape functions.
b) The governing equations (i.e. dynamic equilibrium) are solved at the nodes to calculate the value of updated nodal velocity.
c) Updated values are mapped back to the MPs. See maroon arrows.
d) The velocity and position of the MPs are updated, and the computational grid is reset. In this phase, the compatibility equation and the constitutive equation are also evaluated to update the strain and the stresses at the MPs. The gray dots represent the initial positions, while the black dots represent updated positions. See pink arrows.

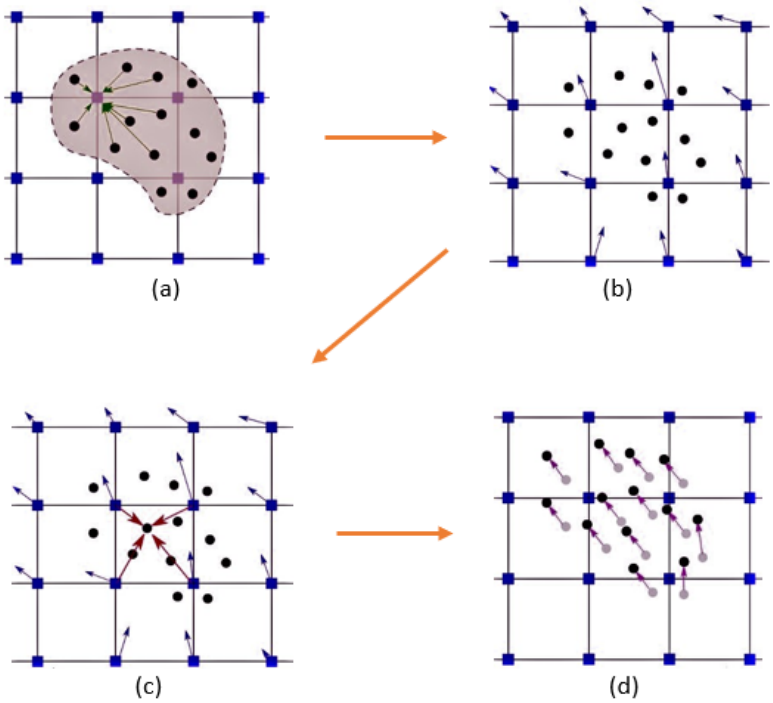

Figure 2.1: Illustration of MPM algorithm (Soga et al., 2016)

2.1.3 Advantages and drawbacks of MPM

The following are the advantages of the MPM:

- Suitable to model large deformation problems without mesh tangling, especially in geotechnical engineering phenomena such as landslides.
- Accurate transfer of material properties via the motion of material points, which allows utilization of history-dependent constitutive models.
- High resemblance to classical FEM. Governing equations and similar knowledge from FEM can be used appropriately applied here, which makes MPM implementation intuitive to FEM users.
- Involves continuum behavior of soil and hence implementing constitute models is "easy".
- Computationally less expensive than other meshed based methods because re-meshing is not required after transferring information from material points to grid nodes.
- Implementation of contact algorithm is intuitive.
- MPM can handle coupled hydromechanical models well.

The following are the drawbacks of MPM:

- Computationally expensive because information needs to be transferred twice (from MPs to nodes and back to MPs) every time step.
- Low-order elements are used hence a first-order accuracy of the velocity is expected.
- Numerical instabilities in the stresses when MPs cross from one element to another (i.e., grid-crossing error) reduce the accuracy of the simulation. This issue can be minimized by using different technics.
- The time integration is usually explicit hence the calculation is conditionally stable.

2.2 Validation of MPM with physical experiment

In this section, we attempt to validate the Material Point method with a lab experiment conducted by Mancarella and Hungr (2010). The experimental setup consists of a 29° downward slope followed by a 33° run-up slope. In that physical model, dry sand is placed at the top of the 29° incline. Specifically, a volume of 0.027 m^3 of sand is positioned in a box with a triangular cross-section at the top. Once released, the granular material flows down to the bottom of the slope and then climbs up the 33° upward ramp.

The basic geometry and material parameters are taken directly from the physical experiment (See Fig 2.2 and Table 2.1). The model is considered in plain-strain conditions, hence the width of the original model (0.35 m) is not considered. The radius of curvature is 0.10 m at the point of change of slope in the lowest part of the incline.

The model is discretized into a fine mesh (mean element size 0.02 m) that would accurately analyze the problem with reasonable computational cost. The model has a total of 19,809 elements and 9,498 nodes. Initially, 20 MPs per element are initiated in the soil domain and the basal material is represented with 4 MPs per element. This is a total of 364,484 MPs. Regarding boundary conditions, the bottom is fully fixed, and the lateral surface on the right is simulated with rollers (only vertical movement is allowed). The interaction between the sand and the base material is simulated using a frictional contact algorithm. The base friction coefficient (μ) is 0.2. The linear elastic – perfectly plastic Mohr-Coulomb constitutive model is considered to model the sand behavior. For simplification, no dilatancy is considered for the soil. It may be noted that dilatancy could affect initial failure mechanisms, but its effect is expected to diminish with the forward motion of soil. In any case, further investigation should be performed in future works.

Figure 2.3 presents a comparison between laboratory data and numerical results. The flow profiles at times 0.6, 1.2, and 2.0 seconds after the soil is released are illustrated. It can be noted that there is a good agreement of the run-out for these time steps, up to 1.2 seconds. At t = 2.0 seconds, we can see that MPM predicts a slightly higher run-up for the model. This could be because the constitutive model used in this case (Mohr-Coulomb model) might be too simplistic to accurately predict the grain-to-grain interaction.

Table 2.1: Material parameters of numerical model used for validation

Parameter	Value
Density of solid particles, ρ	2673 kg/m^3
Porosity, n	0.39
Friction angle of soil, φ	30.9°
Young's modulus, E	500 kPa
Poisson ratio, ν	0.2
Friction coefficient at base, μ	0.4

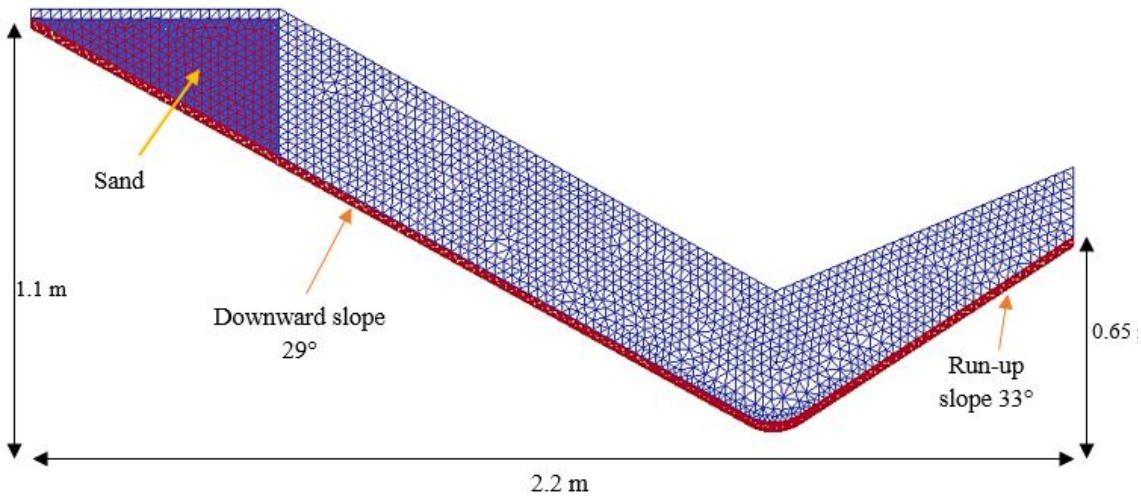

Figure 2.2: Numerical model depicting geometry and discretization of the experimental setup

(a) t = 0.6 seconds after releasing sand

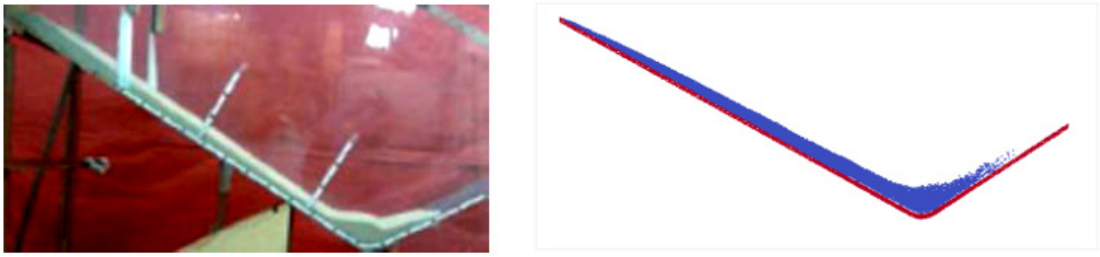

(b) t = 1.2 seconds after releasing sand

(c) t = 2.0 seconds after releasing sand

Figure 2.3: Comparison of the sand motion down the incline from Mancarella and Hungr (2010) experiment (on the left side) with the MPM results (on the right side) at three different times.

3 Numerical modeling of compound landslides using MPM

3.1 Introduction

In the previous section, we validated the MPM framework with a physical laboratory experiment and observed that MPM has the capability to simulate large deformations and can predict the displacement of soil particles moving on a slope with relatively good accuracy. In this section, we extend the use of MPM to explore the development of internal shearing mechanisms in compound landslides

First, we present a general theoretical model of a compound landslide and define the geometrical parameters and physical properties. This general model will serve as a reference for all other subsections in this study. We start by identifying what are the patterns of internal shear mechanisms for various slope transitions. Then, a parametric analysis is performed to observe the effect of basal friction and slope angle on internal shear patterns. Moving further, material degradation is qualitatively evaluated in terms of cumulative deviatoric strain for different geometries. Then, the impact of the landslide against a vertical rigid wall is analyzed in terms of reaction force. Finally, we present a preliminary analysis of the role of protective barriers in mitigating landslide damage.

3.2 General numerical model

In this section, a plane-strain model of a theoretical compound biplane landslide is considered (Figure 3.1). The soil rests on an incline, which makes an angle of θ with the horizontal. The angle of the soil surface at the toe with the horizontal is β, and b is a representative measure of the thickness of the landslide which is measured from the kink in the direction perpendicular to the soil surface. The slope transition is defined by the radius of curvature (R), which is expressed in multiples of b as $R = n \cdot b$, being n the multiplication factor. The basal sliding surface has a friction coefficient of μ and it is included in the model by using a contact algorithm. The soil on the horizontal plane has length *x*, and vertical height *h* on the incline. The total length and height of the model are *X* and *H,* respectively. The radius of the slope transition *(R)*, the basal friction coefficient (μ), and the slope angle *(θ)* will be varied later to study their effects in the internal shear mechanism.

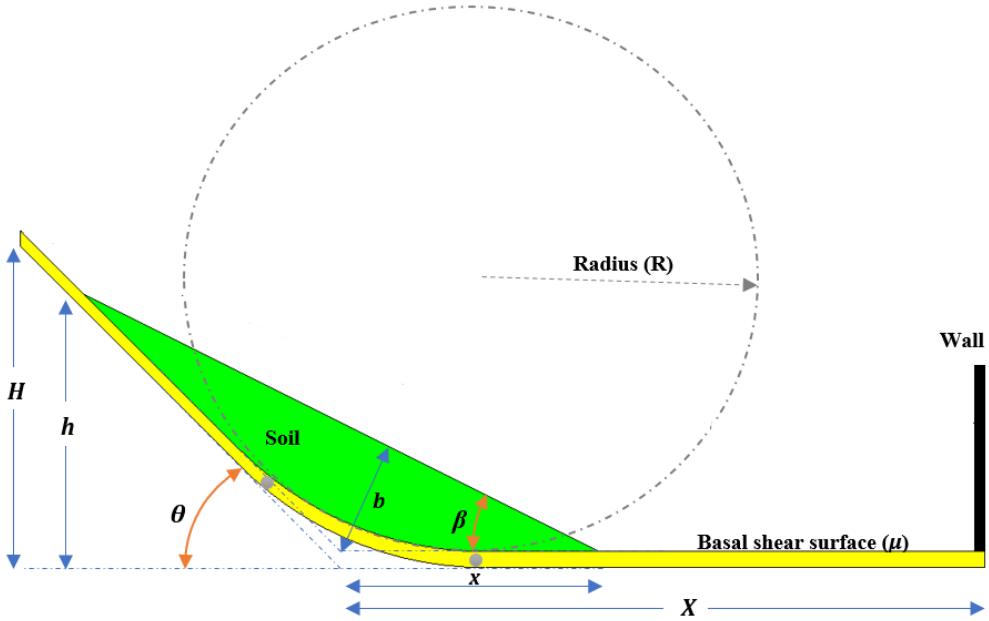

Figure 3.1: General landslide geometry with radius of curvature (*R*)

A vertical wall is placed at the right end of the model on which the magnitude of the impact forces exerted by the moving mass can be measured. The wall is assumed rigid and fully rough which means that no sliding is allowed. The reaction forces on the wall will be calculated to qualitatively analyze energy dissipation phenomena, as discussed in Sections 3.5 and 3.6.

The linear-elastic perfectly-plastic Mohr-Coulomb constitutive model is used to simulate the constitutive behavior of the soil. The soil is assumed frictional and dry (c = 0.01 kPa, ϕ = 35°). See Table 3.1 for material properties. These properties remain the same for landslide models considered in this study.

Table 3.1: Material parameters for soil and basal plane

Material Parameter	Value of parameter	
	Soil	**Basal plane**
Density of solid particles, ρ	2650 kg/m^3	4000 kg/m^3
Porosity, n	0.4	0.4
Young's modulus, E	10000 kPa	20000 kPa
Poisson ratio, ν	0.3	0.33

For all simulations, 4 Material Points (MPs) per element are assigned to the soil material and 1 MP per element to the base material. Regarding boundary constraints, the model is fully fixed at the bottom base and the left and right edges are rollers supported in the x-direction. The mesh size is 0.25 m. This size was found appropriate after performing a mesh convergence analysis, considering the optimization of computational time while maintaining the accuracy of results.

The stresses are initialized with an elastic gravity loading. In this step, the quasi-static convergence is considered and a homogenous damping factor of 0.75 is applied to avoid spurious oscillations. Also, the contact algorithm is off in this initial step assuming fully rough contact between soil and base to avoid sliding. Next, the landslide is triggered by turning on the contact algorithm, hence sliding is allowed and controlled by the friction coefficient μ. During the sliding mechanism, the damping factor is changed to 0.01 to allow for all dynamic effects. The calculation is performed with Anura3D software, and results are analyzed in ParaView.

3.3 Internal shearing pattern

In this section, we plan to gain an initial insight into the formation and evolution of the internal shearing mechanisms in compound landslides. The internal shearing pattern will be described in terms of the landslide parameters (e.g., slope angle, θ, and radius of curvature, R). A parametric analysis is performed to study the effect of the slope transition (R), basal friction resistance (μ), and slope angle (θ) on the development of the internal shear mechanism. Finally, a generalized failure mechanism for compound biplanar landslides is proposed.

3.3.1 Effects of the slope transition

In this section, five slope transitions are analyzed considering different radius of curvature:

- R = 0 (kink slope transition, Figure 3.2)
- R = 0.5*b
- R = b
- R = 1.5*b
- R = 2.0*b

Note that $R = 0$ represents a kink slope transition, with no curvature. Other variables of the model remain constant: $\theta = 45°$, $\beta = 26.5°$, $\mu = 0$, $h = 8\ m$, $x = 8\ m$, $b = 3.58\ m$, $X = 20\ m$, $H = 10\ m$. The assumed value of $\beta = 26.5°$ is small enough to prevent sliding of soil mass over itself during the stress initialization and sufficiently large to occupy soil volume to observe internal shear patterns conveniently. Note that in this section the basal friction is set to zero to maximize the speed of the landslide and reduce the computational time.

3.3.1.1 Kink slope transition: R = 0

The kink slope transition $(R = 0)$ is an abrupt change in slope from an incline to horizontal, 45° to 0° in this case (Figure 3.2). After stress initialization, the contact algorithm is switched on and the soil slides down the incline across the kink. Internal shear bands need to develop to form a kinematically admissible mechanism for sliding to occur. To accurately study the strain localization, we consider several intermediate times during sliding of the moving mass.

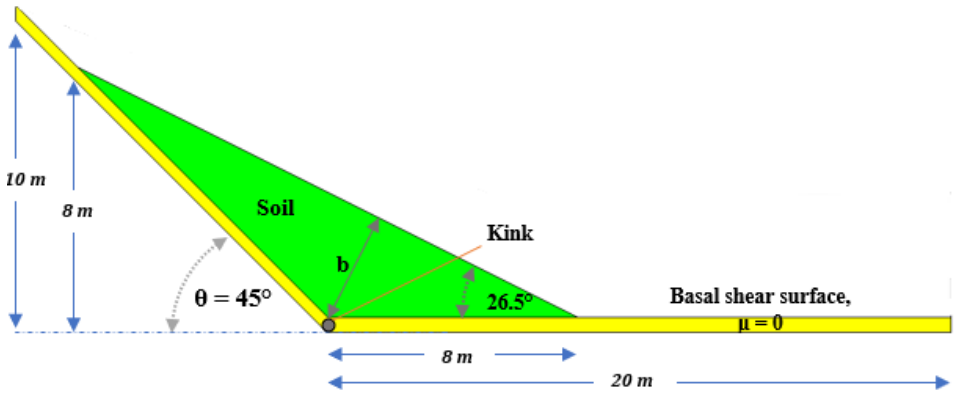

Figure 3.2: Kink slope transition

Figure 3.3 shows incremental deviatoric strain at different times (t = 0.5, 1, 1.5, 2 s). The incremental deviatoric strain is the strain accumulated during a very small fraction of time (time step) of the calculation (5.36×10^{-4} s). This measure allows us to determine the evolution and the location of the internal shear failure mechanisms. At t = 0.5 s, a vertical

shear band develops vertically from the kink and extending to the soil surface. The shearing is more intense at the vertex. The shear band is perpendicular to the basal surface. At t = 1.0 s the shearing becomes more intense as more and more soil passes through the initial vertical shearing plane and a triangular shear region starts to develop. At t = 1.5 s, a triangular shear band is observed with the vertex at the kink, and edges almost normal to the slip surfaces. The angle that defines the internal failure mechanism (α) is about 45°, which coincides with the slope angle (θ). Finally, at t = 2.0 s, the triangular shear zone is slightly wider, $\alpha \approx 55°$, which can be represented in terms of the slope angle as: $\alpha \approx \theta + \alpha'$, where α' ranges from 0 – 10°. The incremental angle α', is possibly created due to the forward movement of soil on the horizontal plane.

As soil passes through the kink, the region of strain localization becomes more triangular after starting from a vertical shape. The material is hence more sheared as it reaches the other side of the shear band. Therefore, energy dissipation also takes place in this process.

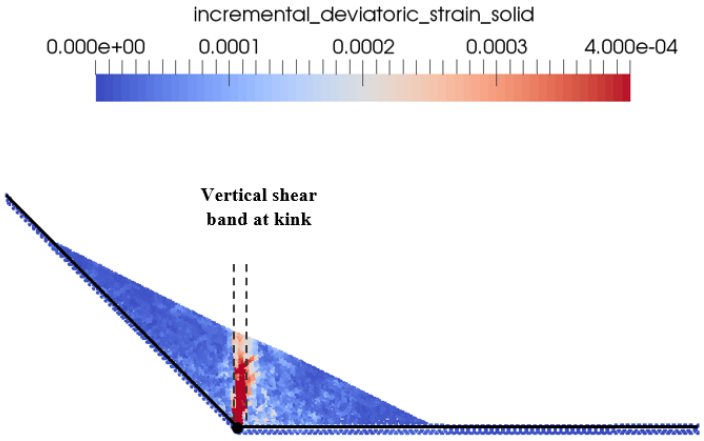

(a) t = 0.5 sec

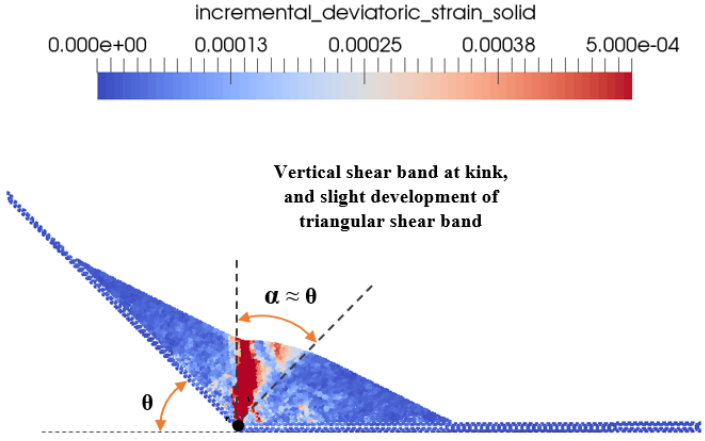

(b) t = 1 sec

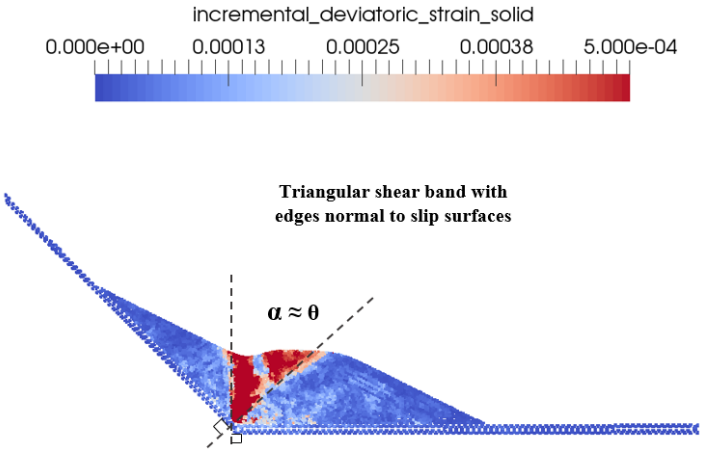

(c) t = 1.5 sec

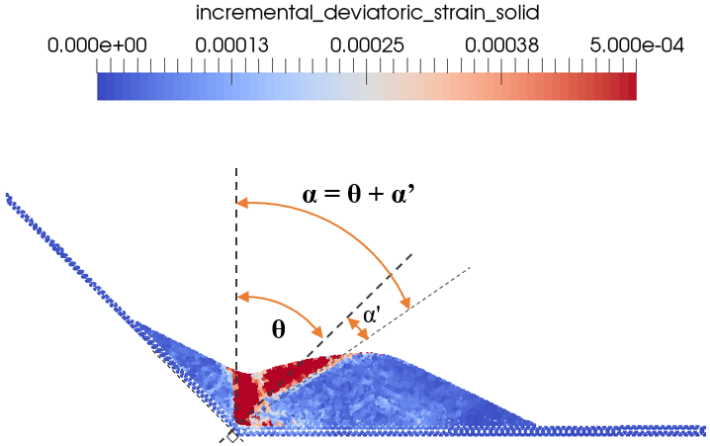

(d) t = 2 sec.

Figure 3.3: Internal shearing mechanism for a compound landslide with kink slope with geometry at different time intervals

3.3.1.2 Curved transition: R = 0.5b

In this model the slope transition is curved, the radius of curvature is half the maximum thickness of the landslide (b), i.e. $R = 0.5b = 1.79$ m (Figure 3.4).

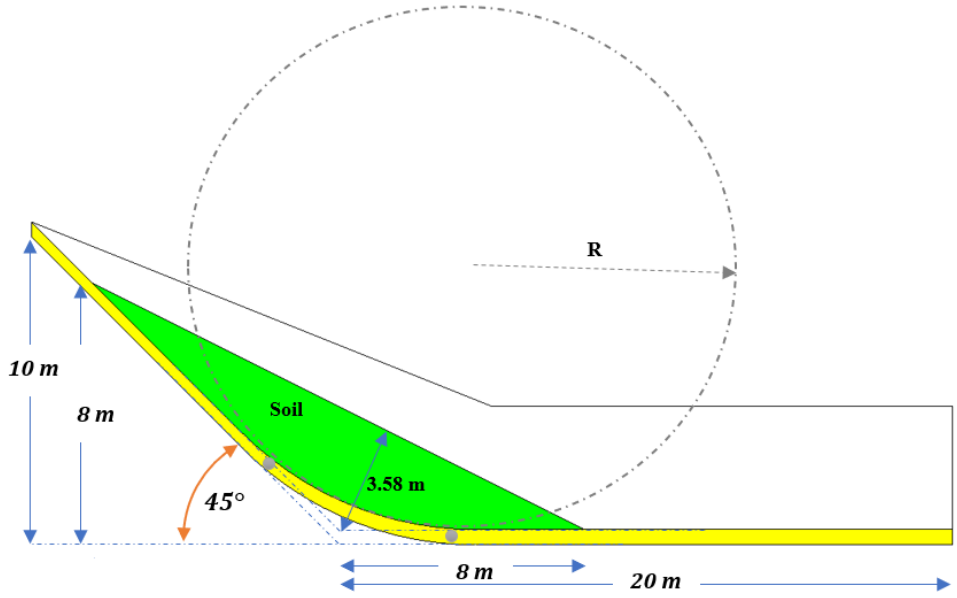

Figure 3.4: General numerical model for a curved landslide geometry

Figure 3.5 depicts the evolution of the internal shear patterns at four times. At t = 0.5 sec, a vertical shear band is developed and a minor second shear band is also observed normal to the incline. Despite these shear bands seem to originate around the slope transition, the material located just above the curvature seems to remain unsheared. At t = 1.0 s and 1.5 s, a vertical shear zone develops vertically from the first point of the curved transition. Also, a triangular sheared region develops with the vertex at end point of the slope transition and the sides perpendicular to the basal slope planes ($\alpha \approx 45°$). Finally, at t = 2 s, the same failure mechanism is observed but the triangular sheared zone slightly widens and the shear angle becomes $\alpha \approx 55°$.

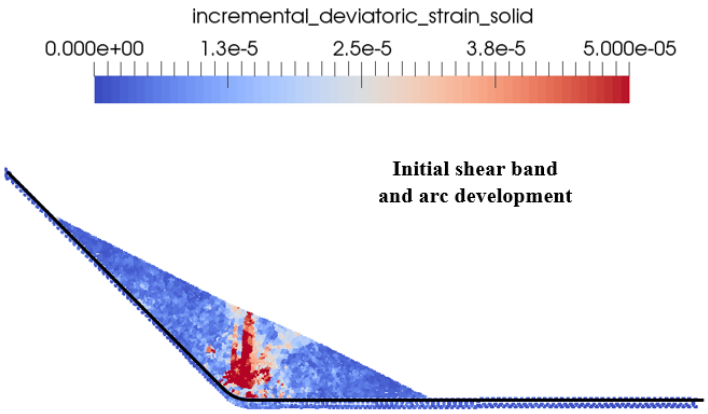

(a) t = 0.5 sec

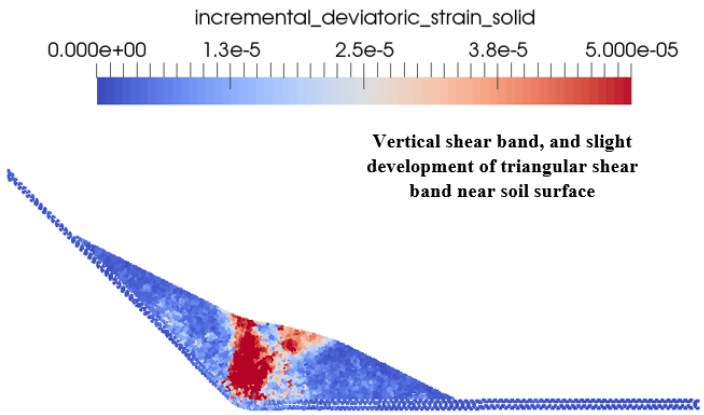

(b) t = 1 sec

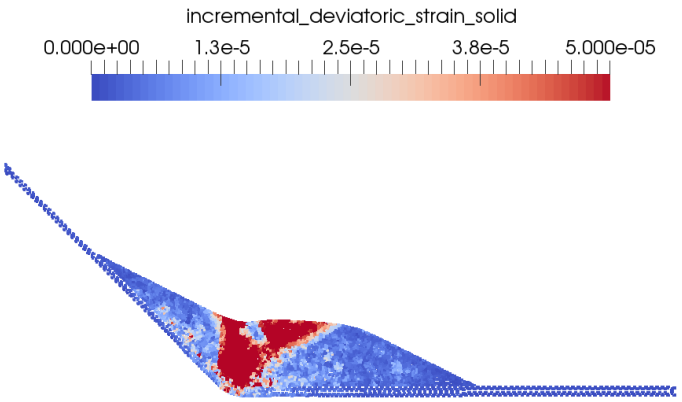

c) t = 1.5 sec

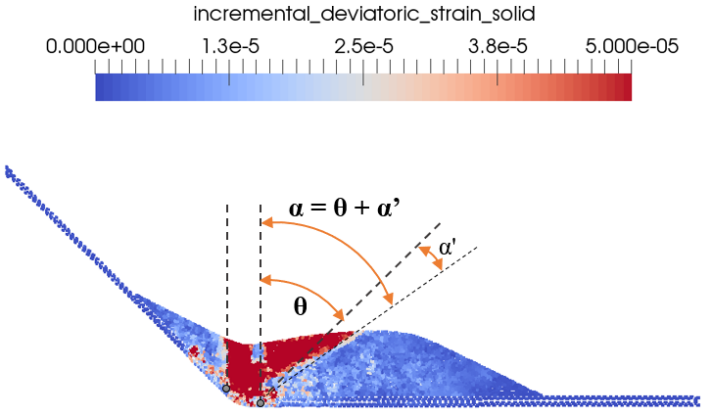

(d) t = 2 sec.

Figure 3.5: Internal shearing mechanism for landslide (R = 0.5*b) at different time intervals

3.3.1.3 Curved transition: R = b

The radius of curvature in this model is 3.58 m, equal to the maximum thickness *(b)* of the soil. The evolution of the incremental deviatoric strain is presented in Figure 3.6. At t = 0.5s, two shear zones develop from the two edge points of the curved transition towards the soil surface. Also, a shear arc is distinguished. The shear arc has its end points at the start and end of the curvature, and the soil just beneath the transition zone is not sheared. At t = 1.0 s and 1.5 s, two triangular shear regions are seen with vertices roughly starting at the end points of the curved transition, and edges normal to the incline and horizontal surfaces, respectively. The sheared angles of the triangular zones are approximately the same, $\alpha \approx 45°$. A shear arc connects the vertex of the two triangular sheared zones, at the end points of the curvature. At t = 2.0 s, the same shear pattern is observed. While the first shear triangular region on the left keeps shrinking as soil flows forward, the second region gets larger due to more soil accumulation. The angle α is about 45° for the initial shear band. The second shear band on the right has a small increment α' of about 10° which makes the total angle α equal to nearly 55°.

In this particular case, the radius of the shear arc measures $d \approx 1.5$ m. Using trigonometry (Figure 3.7), the measured radius *(d)* can be expressed in terms of slope parameters (i.e., R and θ) as follows:

$$\mathrm{d} = \mathrm{k}\,\mathrm{R}\tan(\theta/2) \qquad \text{(Equation 1)}$$

with *k* being a factor. Also, it can be expressed as $\mathrm{d} = \mathrm{k}\,\mathrm{r}$, where $r = R\,tan(\theta/2)$

In this case, $\mathrm{r} = 3.58 * \tan 22.5° \approx 1.5$ m. This value coincides with the measured radius of the shear arc d . So, $d \approx r$, hence $k = 1$. This means that the center of shear arc roughly coincides with theoretical kink in this case.

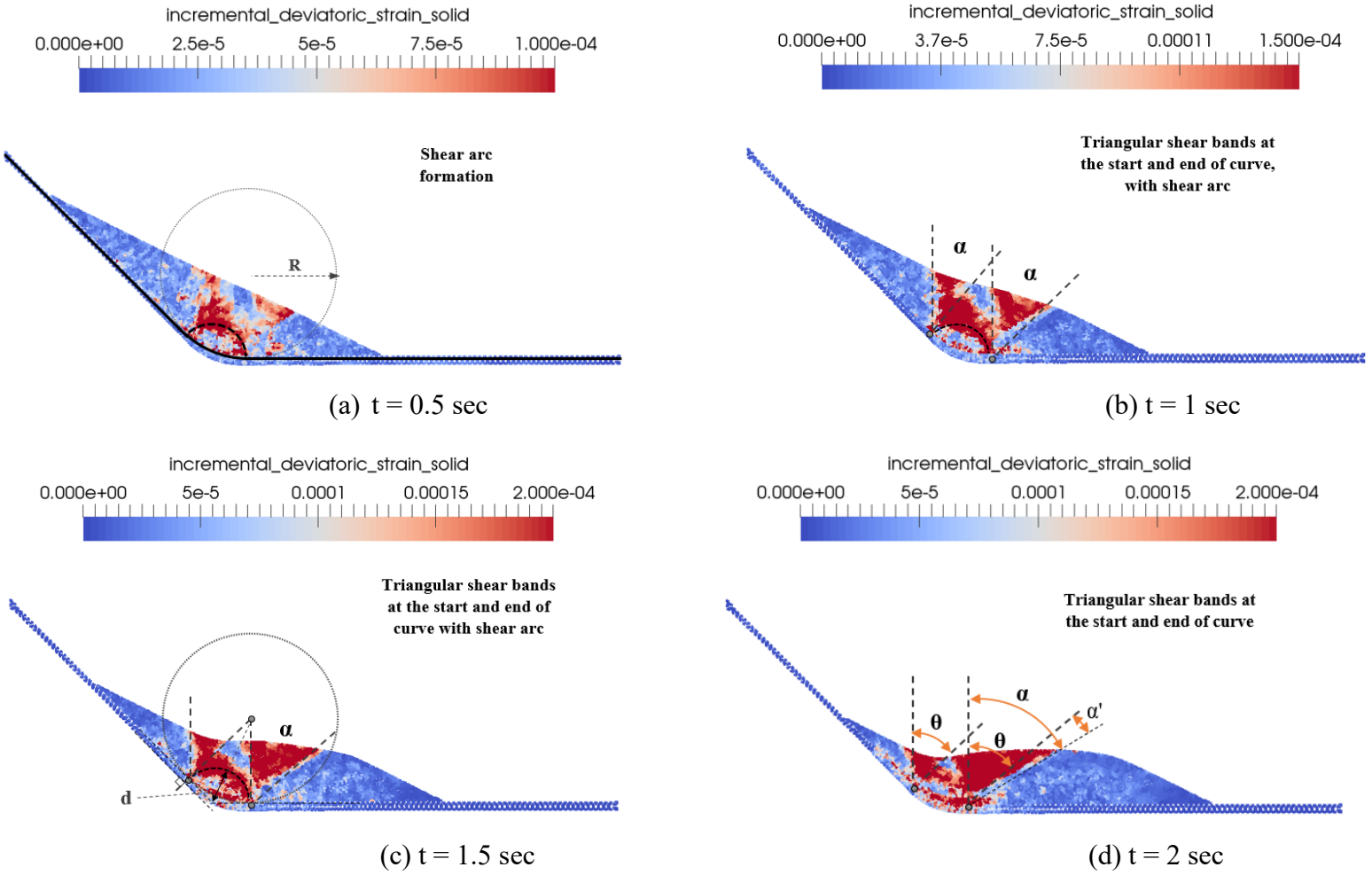

Figure 3.6: Internal shearing mechanism for landslide (R = b) at different time intervals

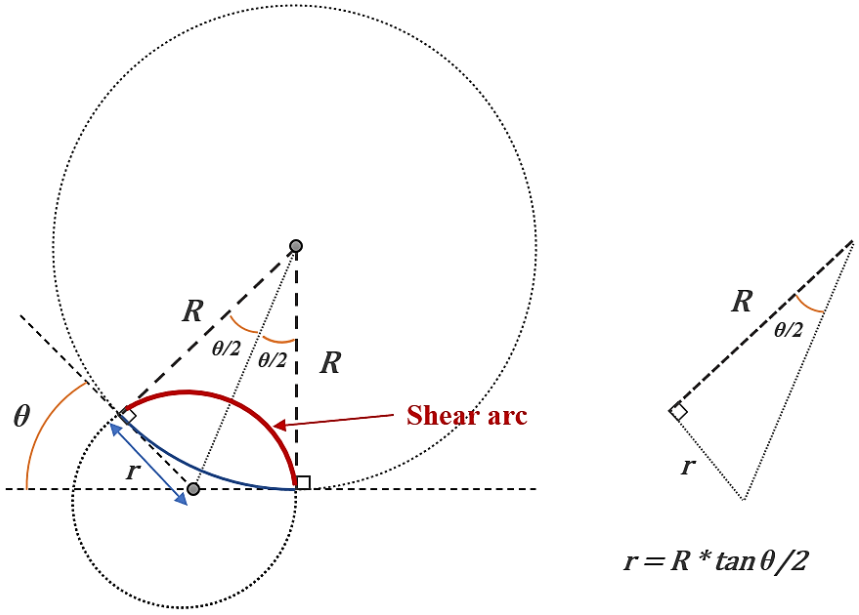

Figure 3.7: Geometrical calculation for shear arc measurements

*3.3.1.4 Curved transition: R = 1.5*b*

The radius of curvature in this case is 5.37 m, equal to 1.5 times the maximum width *(b)* of soil, $R = 1.5b$. The evolution of incremental deviatoric strain is presented in Figure 3.8. At t = 0.5 s, an outline of two localized triangular shear regions are observed, which are connected by an arc. Note that shear bands have not developed fully yet, and appear to originate from the start and end points of the curvature. The radius of shear arc, $d = 2.58$ *m*, which is 0.48 times the radius of curvature (R). Analytically, radius of shear arc, $r = 2.22$ *m*. From our assumption of $d = k*r$, the value of $k = 1.16$ in this case.

At t = 1.0 s, two distinct triangular shear bands are seen with angle $\alpha = 45°$. A shear arc (outlined in black) is also observed. At t = 1.5 s, α is about 45° for the initial shear band. For the second shear band, a small increment $\alpha' \approx 10°$ is present, which makes α equal to nearly 55°. At t = 2 s, the same shear pattern is observed. The first triangle becomes smaller with time, and the size of second one increases. In all cases, we note the presence of basal accumulation of shear along the curvature. The angle α is roughly 55°, with $\alpha' \approx 10°$.

3.3.1.5 Curved transition: R = 2b

The radius of curvature is $R = 2b$ = 7.16 m, which is the largest of all radii that we consider in this section. Figure 3.9 depicts the various stages of incremental deviatoric strain. At t = 0.5 s, triangular shear bands start developing at the end points of the curvature. The radius of shear arc, $d = 3.3\ m$, which is approximately 0.46 times the radius of curvature. Analytically, $r = 7.16 * \tan 22.5° \approx 3.0\ m$. From the assumption of $d = k*r$, the value of k is 1.1 in this case.

At t = 1.0 s, two distinct triangular shear bands are observed extending from the end points of curvature. The shear arc is faint and hard to visualize. The included angles of these shear bands are 45° and 53° respectively. Small increment angle $\alpha' \approx 8°$. At t = 1.5 s, similar shear pattern is observed with the angles being 45° and 55°. The increment $\alpha' \approx 10°$ due to forward motion of mass. The shear arc is faintly visible, connecting the two shear bands. At t = 2.0 s, the first shear band has shrunk in size and the second one has become larger. Shear arc is not visible and is most likely outside the soil surface at this moment. The first shear band on the slope includes an angle $\alpha = \theta = 45°$, while the second shear band on the horizontal plane includes an angle $\alpha \approx 55°$

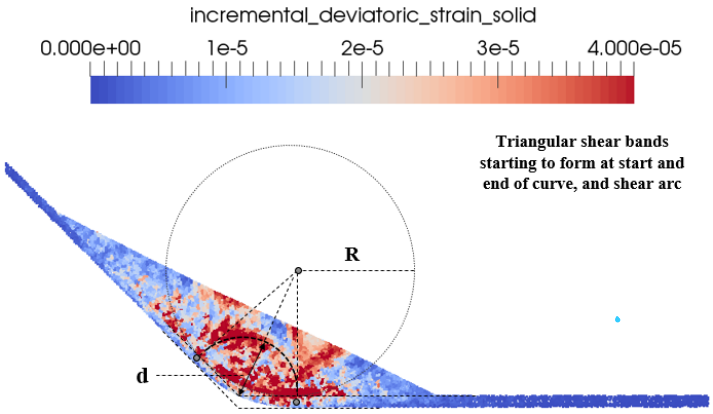

(a) t = 0.5 sec

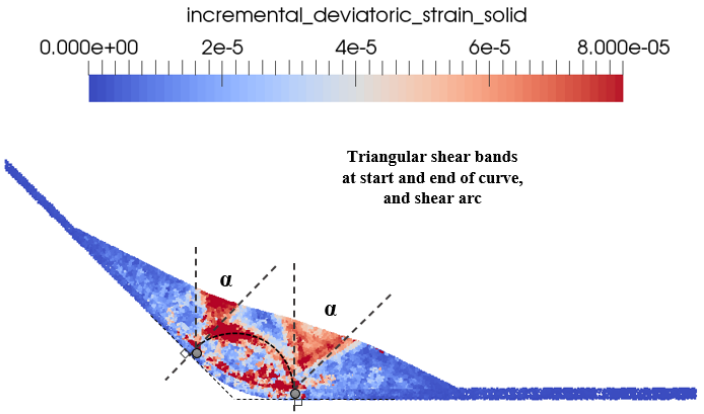

(b) t = 1 sec

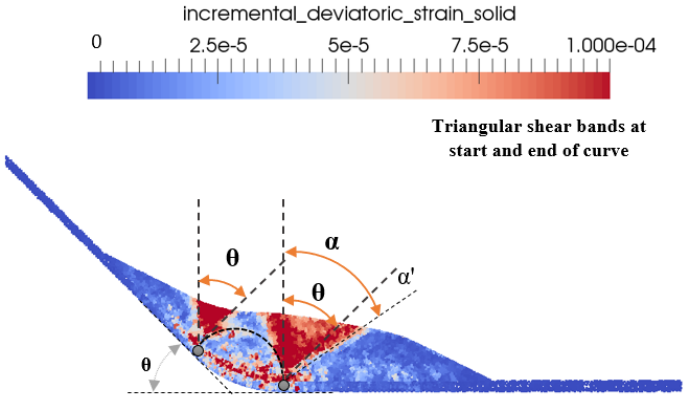

(c) t = 1.5 sec

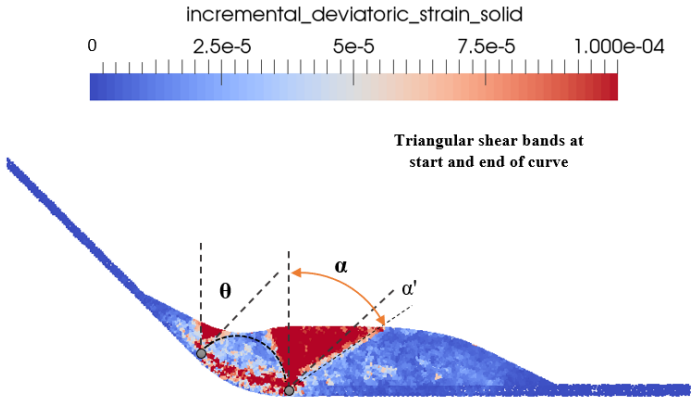

(d) t = 2 sec.

Figure 3.8: Internal shearing mechanism for landslide (R = 1.5*b) at different time intervals

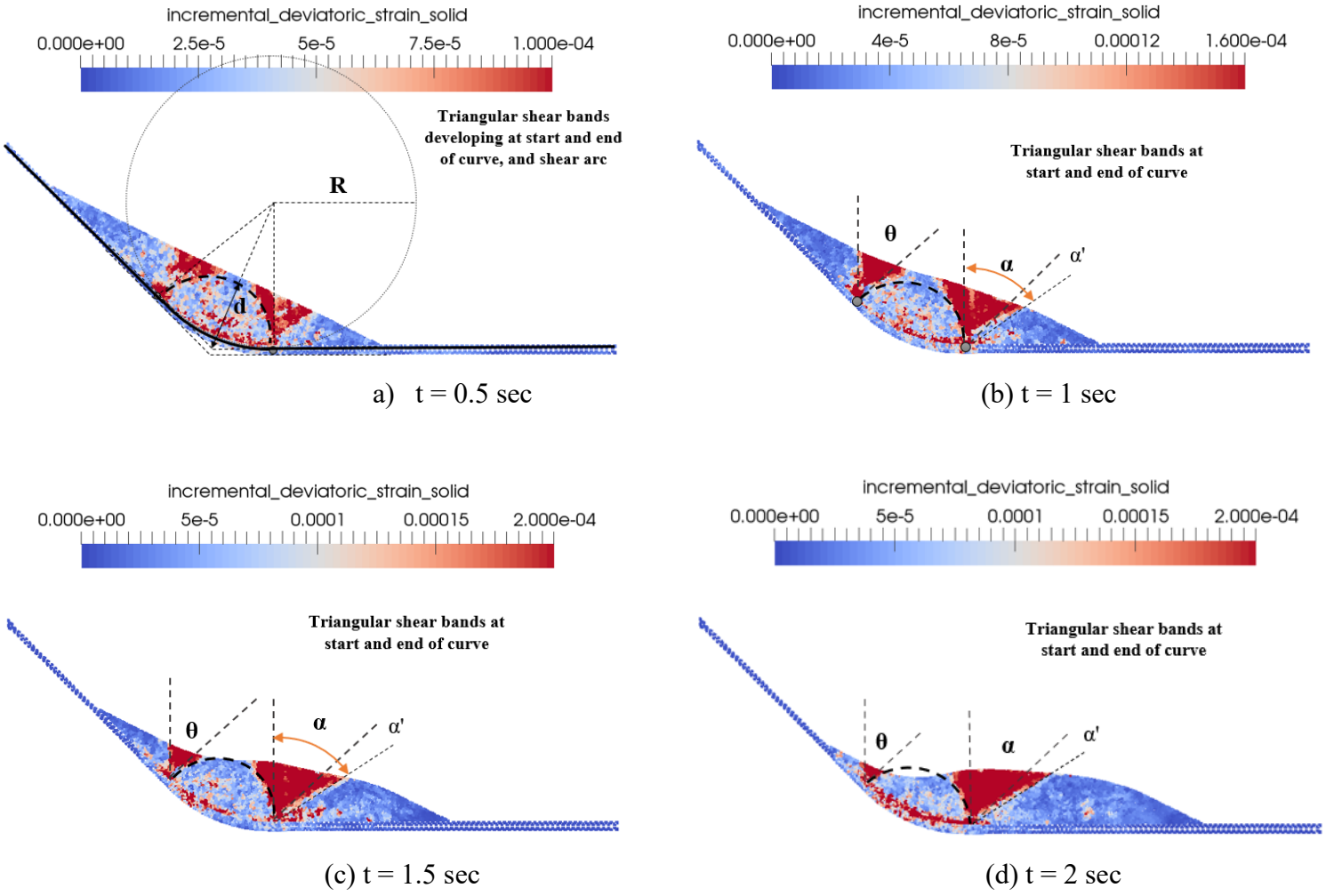

Figure 3.9: Internal shearing mechanism for landslide (R = 2*b) at different time intervals

3.3.1.6 Key findings regarding slope transition

In this section, the internal shear mechanism was studied for a compound landslide with a slope angle of 45°. Incremental deviatoric strain was used to identify the regions of momentary strain localization for different geometries. It can be observed that as the soil slides down the basal surface triangular shear bands develop from the two points where the slope changes perpendicular to the slope surfaces. This can be explained because the velocity field in the sliding mass is affected by the changes in slope at the basal surface, from a rectilinear movement to a circular movement and vice versa. On top of the two triangular shear zones, a shear arc connects both zones which indicates the rotation of the sliding mass near the slope transition. The totality of these shear bands forms a kinematical admissible failure mechanism. A summary of the numerical results is presented in Table 3.2.

Despite having different basal geometries, a generalized internal shear mechanism can be defined in terms of the shearing angle α of the triangular regions and the radius of the shear arc (d). Both parameters are related to the slope angle θ and radius of curvature of the slope transition R as follows:

- Shearing angle: $\alpha = \theta + \alpha'$ (Range of α': 0 – 10°, increases with the direction of the motion)
- Radius of the shear arc: $d \approx k * r$, where $r = R \ tan\ (\theta/2)$ (Range of k: 1.0 – 1.2)

Note that the kink slope transition $(R = 0)$ becomes a particular case of the proposed general mechanism.

In Figure 3.10 the internal failure patterns are presented for three different R at two different times (t = 1 s and t = 1.5 s). From this plot, it can be observed that the magnitude of the incremental deviatoric strain increases for smaller R.

Finally, it is important to highlight that the general shearing pattern observed here is consistent with field data from Glastonbury and Fell (2010), who observed that the internal shear bands were generally perpendicular to basal sliding planes.

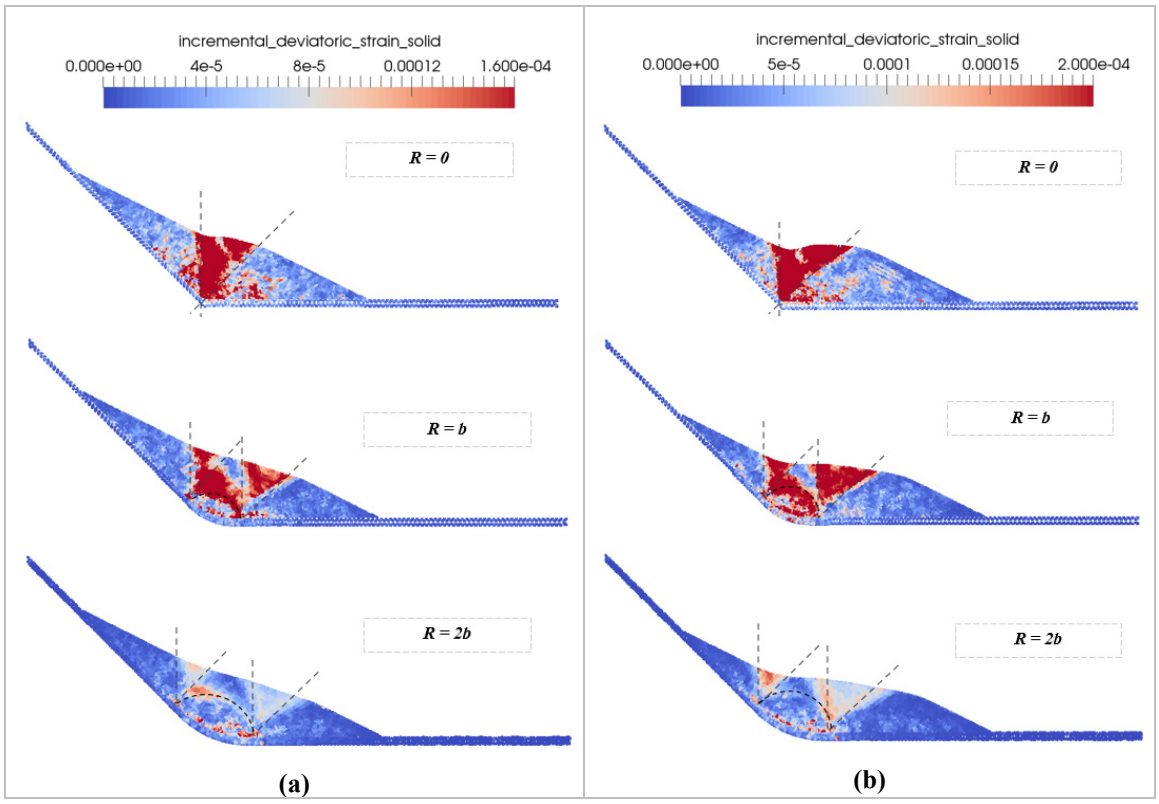

Figure 3.10: Incremental deviatoric strain at (a) t = 1 s and (b) t = 1.5 s

Table 3.2: Summary of geometrical observations for shear bands (θ = 45°, b = 3.58 m)

Radius (R) of slope transition	Number of shear bands	Location of shear bands	Angles of shearing (α)	Measured shear arc (d)	Remarks
$R = 0$	1 triangular region	At kink	Initially, $\alpha = \theta = 45°$ Finally, $\alpha \approx 55° = 45° + 10°$ Hence, $\alpha = \theta + \alpha'$ Range of α': $0 - 10°$	No arc formed	-
$R = 0.5*b$ (1.78 m)	1 triangular region	At end of curve		Shear arc difficult to see	-
$R = b$ (3.57 m)	2 triangular + shear arc	At start and end of curve. Shear arc in between		d = 1.5 m	$d = 0.42*R$ $d = r$
$R = 1.5*b$ (5.37 m)	2 triangular + shear arc			d = 2.58 m	$d = 0.48*R$ $d = 1.16*r$
$R = 2*b$ (7.16 m)	2 triangular + shear arc			d = 3.3 m	$d = 0.46*R$ $d = 1.1*r$

3.3.2 Effect of basal friction resistance

Cases with frictionless $(\mu = 0)$ basal shear surfaces were analyzed in the previous section to optimize results and make calculations faster. In this section, the effect of the basal friction resistance (μ) on the slip surface is studied keeping all other parameters the same as discussed in Section 3.1. A non-zero friction coefficient ($\mu = 0.08$ *and* 0.17) is assigned to the slip surface to check if it alters the shearing mechanism of the compound landslide observed in the previous section. Note that higher values of friction coefficient are not considered because the landslide final runout becomes too small.

Hereinafter, we use the parameter ψ to denote the contact friction angle between the soil and basal shear surface, where $\mu = \tan \psi$.

3.3.2.1 Friction coefficient, μ = 0.08

A friction coefficient of $\mu = 0.08$ (corresponding to a basal friction angle of $\psi = 5°$) is assigned to the basal slip surface. The simulation is run for the model with $R = 1.5 * b$, because both the shear bands and shear arc were clearly visible in section *3.3.1.4*. Figure 3.11 shows the internal shear band formation when toe is 10 m and 6 m away from the edge of the model. The general mechanism obtained for the frictionless case is superimposed on top that of this figure, which is in good agreement with the internal shearing bands, being $\alpha \approx 45° = \theta$ and $d = 2.55$ m, $r = 2.22$. Setting $d = k\,r$ gives $k = 1.15$. Something important to be noted is that with the advancement of the landslide, α slightly increases (Figure 3.11b).

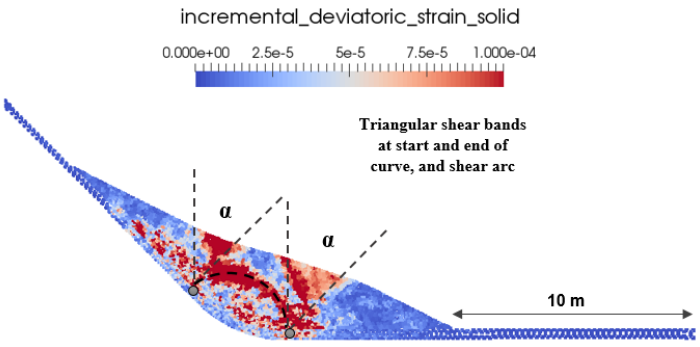

(a)

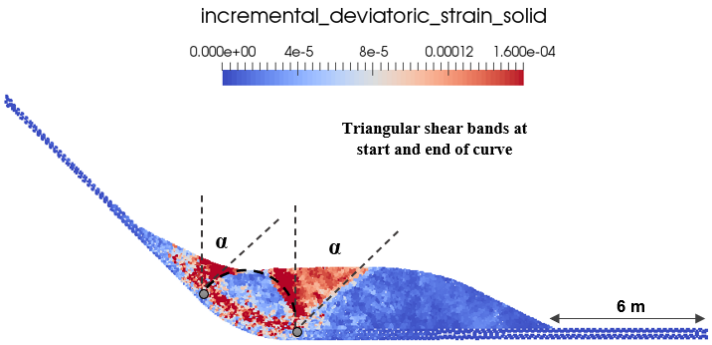

(b)

Figure 3.11: Internal shear bands when toe is a) 10 m and b) 6 m from the model edge (μ = 0.08)

3.3.2.2 Friction coefficient, μ = 0.17

A friction coefficient of $\mu = 0.17$ (corresponding to a basal friction angle of $\psi = 10°$) is assigned to entire the slip surface. Again, the case with $R = 1.5 * b$ is analyzed and after superimposing the mechanism proposed in section 3.3.1. In Figure 3.12, we see that the observed internal shearing pattern matches reasonably well. With the movement of the soil mass, α does not seem to increase. $d = 2.55$ m with $k = 1.15$.

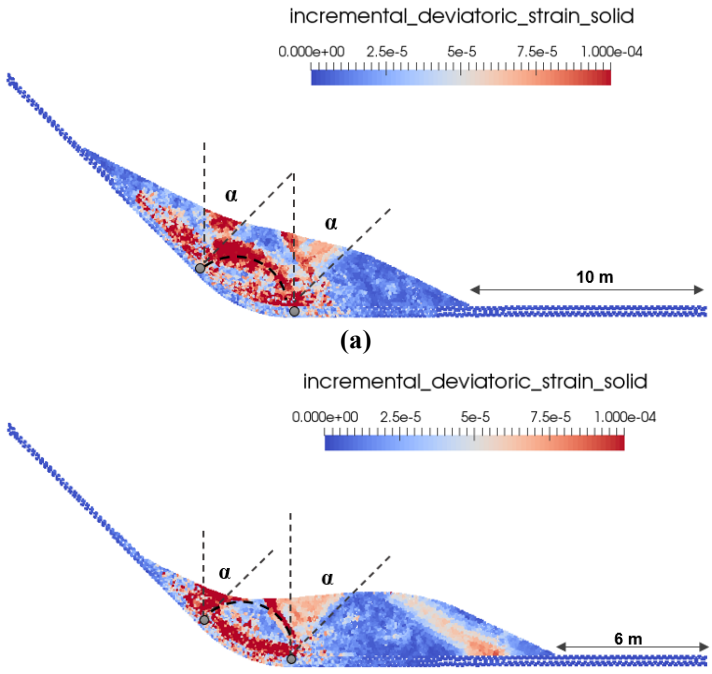

(a)

(b)

Figure 3.12: Internal shear bands when toe is a) 10 m and b) 6 m from the model edge (μ = 0.17)

It is noted that the landslide stops and stabilizes before reaching the end wall. We also see a shear band occurring near the toe almost parallel to the surface. This might be due to the difference in velocities of particles of the moving mass. Due to internal shear, some particles possess a lower velocity than neighboring ones and come to rest earlier than neighboring particles due to friction, causing a shear band to develop near the toe of the landslide.

3.3.2.3 Key findings regarding basal friction resistance

In Table 3.3, we compare the internal shearing mechanism of a landslide with rounded geometry *(R = 5.37 m)* for three cases with basal friction $\psi = 0°, 5°, 10°$. The incremental deviatoric strain is plotted for toe distances 10 m and 6 m from the end, and following points are noted:

- For 10 m distance, the angles in all models are roughly: $\alpha = 45°$.
  For 6 m distance, the angles for frictionless model are: $\alpha = 45 - 55°,\ \alpha' \approx 0 - 10°$.
  For the friction model, they are: $\alpha = 45°,\ \alpha' \approx$ 0-10°. We note that there is a 5 – 10° decrease in the total value of α, which could be due to more resistance to motion offered from the basal shear surface during forward motion of soil. So,

  $$\alpha = \theta + \alpha' - \psi \qquad \text{(Equation 2)}$$

  The range of α' is 0 – 10°.
- The radius of shear arc does not seem to be affected by the basal friction resistance, hence the same expression presented in Section 3.3.1 (Equation 1).

$$d\,(\text{when } \psi = 0) \approx d\,(\text{when } \psi \neq 0)$$

From the above analysis, we can comment that the basal friction does not have a significant change in internal shearing mechanism. The shape of the shear bands remains very similar, with minor changes in α. The change is nearly equal and opposite to the included friction.

Table 3.3: Comparison of frictionless and friction models

Distance of toe from end	$\mu = 0$ ($\psi = 0°$)	$\mu = 0.08$ ($\psi = 5°$)	$\mu = 0.17$ ($\psi = 10°$)
10 m	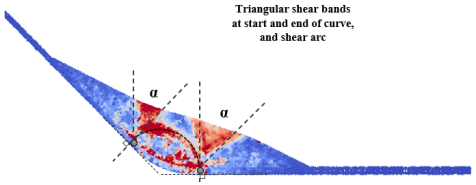 $\alpha = 45°,\ \alpha' \approx 0°$ $d = 2.58\ m$	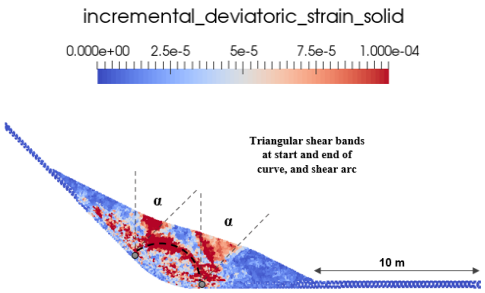 $\alpha = 45°,\ \alpha' \approx 0\text{-}5°$ $d = 2.55\ m$	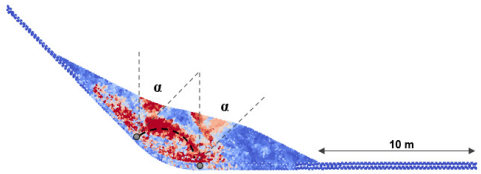 $\alpha = 45°,\ \alpha' \approx 0\text{-}10°$ $d = 2.55\ m$
6 m	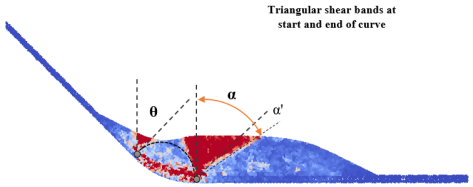 $\alpha = 45\text{-}55°,\ \alpha' \approx 0 - 10°$	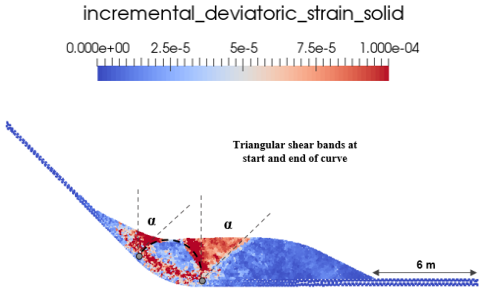 $\alpha = 45\text{-}50°,\ \alpha' \approx 0\text{-}5°$	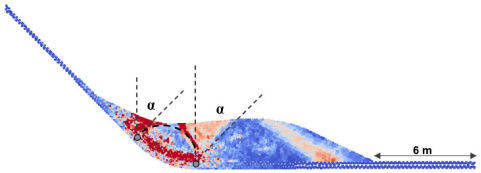 $\alpha = 45°,\ \alpha' \approx 0\text{-}10°$

3.3.3 Effect of slope angle

To study the effect of the slope angle θ in development of internal shearing mechanism, we construct two additional configurations are analyzed with slope angles of 37° and 26°. For each slope angle, different slope transitions are accounted. Note that the models from previous sections were performed with θ = 45°.

3.3.3.1 Slope angle, $\theta = 37°$

Figure 3.13 depicts the general model of the landslide geometry. Particularities of the model: $\theta = 37°$, $\beta = 26.5°$, $\mu = 0$, $h = 13.4\,m$, $x = 9.8\,m$, $b = 4\,m$, $X = 15\,m, H = 14.1\,m$. Three slope transitions have been considered: $R = 0$, $R = b$, *and* $R = 2b$.

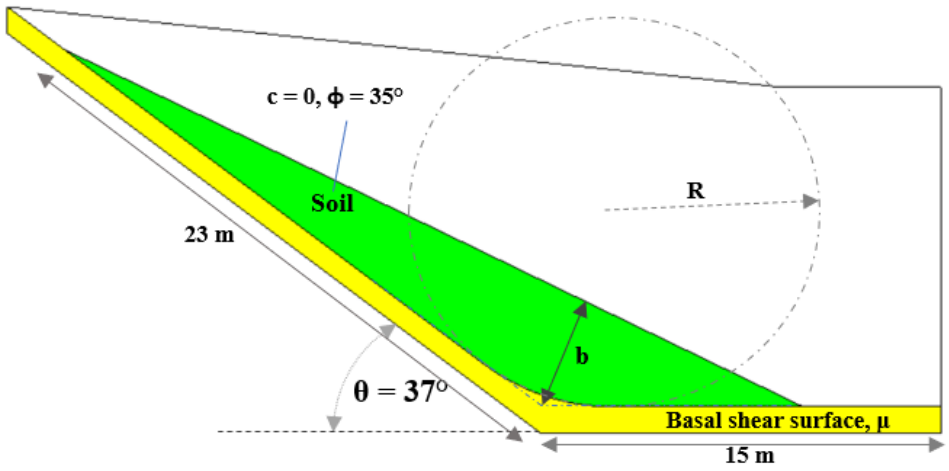

Figure 3.13: General landslide geometry with 37° slope

i. Kink slope transition, $R = 0$, with $\theta = 37°$

Figure 3.14(a) shows the incremental deviatoric strain for a kink slope transition after sliding for 1 second from rest position. This is an initial stage during failure mechanism of this landslide. The shear band is essentially vertical and develops from the kink. At t = 1.5s (Figure 3.14b), the triangular shear band develops similarly to previous cases with the vertex at the kink. The angle of the sheared triangular region α is nearly 47°, which is equal to the slope angle θ, plus an increment $\alpha' = 10°$ in this case.

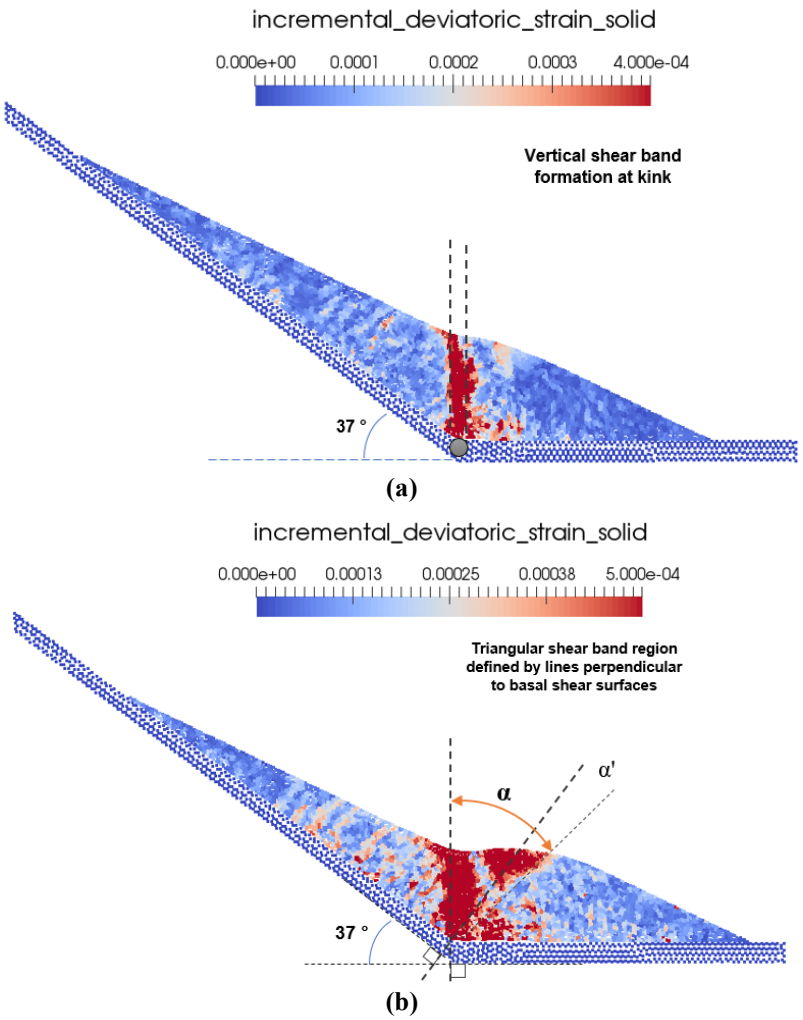

Figure 3.14: Internal shear mechanism at (a) t = 1 sand (b) t = 1.5 sec (R= 0, θ = 37°)

ii. Curved slope transition, $R = b$, with $\theta = 37°$

Figure 3.15 shows the incremental deviatoric strain of a landslide with radius of curvature of 4 m *($R = b$)* after sliding for 1.6 seconds from rest position. This is an intermediate stage during failure mechanism of this landslide. Two distinct triangular shear bands and a shear arc are observed. The edges of the triangular regions are defined by adjacent lines which are nearly perpendicular to the two basal slip surfaces i.e. 37° and horizontal. The included angle α is approximately 37° and $\alpha' \approx 0°$. The radius of shear arc *(d)* is nearly 1.7 m, and $r \approx 1.3$ m, which makes $k \approx 1.3$.

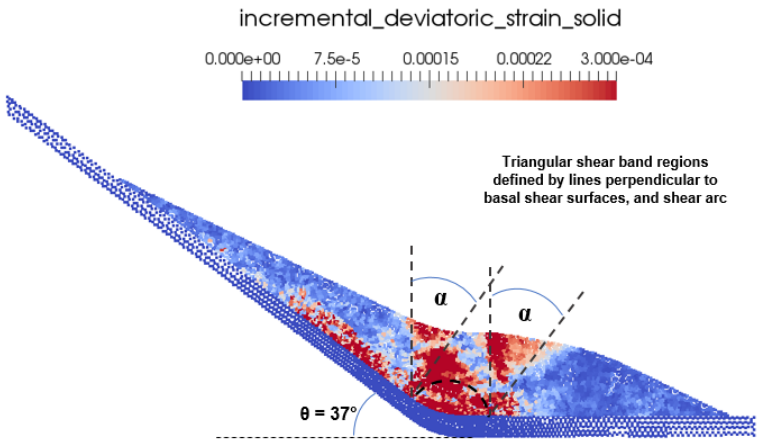

Figure 3.15: Internal shear mechanism at t = 1.6 s for round geometry (R = b, θ = 37°)

iii. Curved slope transition, $R = 2b$, with $\theta = 37°$

Figure 3.16 shows the incremental deviatoric strain of the landslide with a radius of curvature of 8 m *($R = 2b$)* after sliding for 1.5 seconds from rest position. This is an intermediate stage during failure mechanism of this landslide. Two distinct triangular shear bands and a shear arc are observed. The included angle for the first shear band is nearly 37°, which is equal to slope angle θ. For the second shear band, there is a small increment $\alpha' \approx 10°$, which makes $\alpha \approx 47°$. The radius of the shear arc, d is nearly 2.9 m, and $r = 2.52$ m, which makes $k = 1.15$.

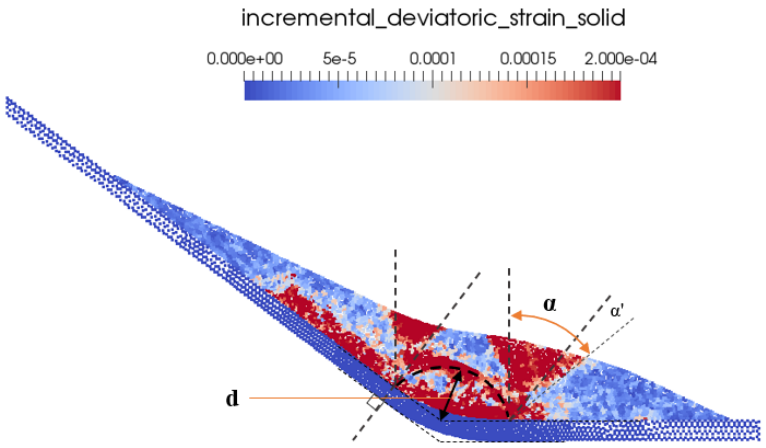

Figure 3.16: Internal shear mechanism at t = 1.5 s for round geometry (R = 2b, θ = 37°)

Table 3.4 summarizes the relation between the slope geometry *(R, θ)*, shear band characteristics and location, angles of shearing *(α)*, and radius of shear arc *(d)*.

Table 3.4: Summary of geometrical observations for shear bands (θ = 37°, b = 4 m)

Radius (R) of transition	Number of shear bands	Location of shear bands	Angle of shearing (α)	Radius of shear arc (d)
$R = 0\ m$ (Kink)	1 triangular region	At kink	Vertical initially. $\alpha \approx 47°$ later.	No arc formed
$R = b = 4\ m$	2 triangular + shear arc	At start and end of curve. Shear arc in between	$\alpha = 37° + \alpha'$ $\alpha = \theta + \alpha'$ Range of α′: 0 – 10°	$d = 1.7\ m$ $d = 1.3*r$
$R = 2b = 8\ m$	2 triangular + shear arc	At start and end of curve. Shear arc in between		$d = 2.9\ m$ $d = 1.15*r$

3.3.3.2 Slope angle, $\theta = 26°$

In this subsection, a landslide with 26° slope is studied. Figure 3.17 depicts the general geometry of the model. The maximum width of soil, $b = 2.6\ m$ in this case. Particularities of the model: $\theta = 26°$, $\beta = 17°$, $\mu = 0$, $h = 8\ m$, $x = 8\ m$, $b = 3.58\ m$, $X = 20\ m, H = 8.5\ m$. Two slope transitions are considered: one with a kink ($R = 0$), and a curved one ($R = 2b$).

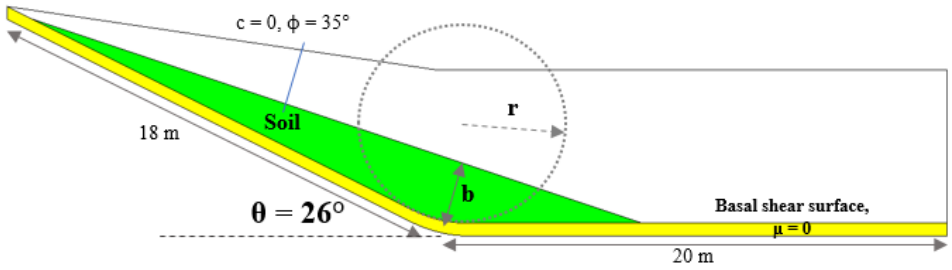

Figure 3.17: General landslide geometry for slope, θ = 26°

i. Kink slope transition, $R = 0$, with $\theta = 26°$

Figure 3.18 shows the incremental deviatoric strain in kink slope transition geometry at time 1.2 s. We superimpose our assumed failure mechanism on top of the figure. From geometrical constructions, $\alpha \approx 36°$, which is equal to sum of θ and increment $\alpha' = 10°$.

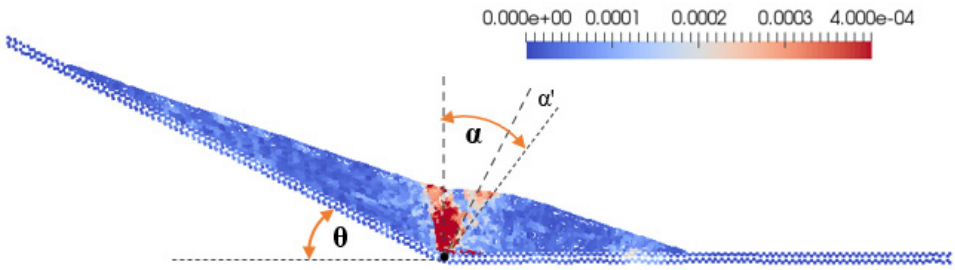

Figure 3.18: Incremental deviatoric strain at t = 1.2 sec for a kink transition (θ = 26°)

ii. Curved slope transition, R = 2b, with θ = 26°

Figure 3.19 shows incremental deviatoric strain with radius 5.2 m ($R = 2b$) at t = 2 s. After superimposing the proposed failure mechanism, we find α to be nearly 36°, which agrees with our assumption, $\alpha = \theta + \alpha'$ with $\alpha' = 10°$. Two shear bands originate from the end points of the curved transition. The shear arc is not clearly visible, which might due to small slope angle θ. Note that the shear magnitude in this case is very small compared to previous simulations.

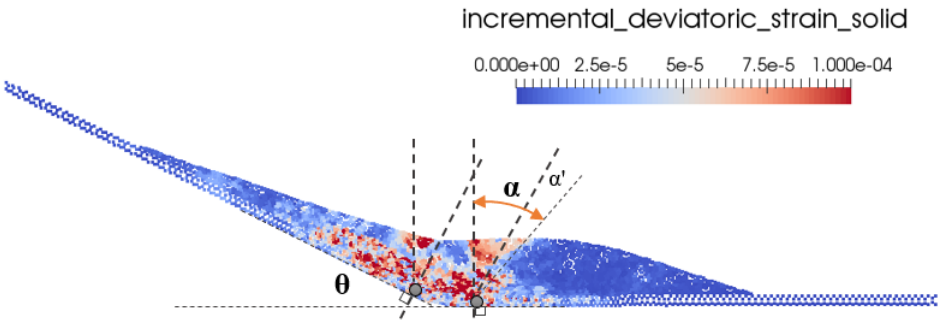

Figure 3.19: Incremental deviatoric strain at t = 2 sec for R = 2b (θ = 26°)

Table 3.5: Summary of geometrical observations for shear bands (θ = 26°, b = 3.58 m)

Radius of slope transition (R)	Number of shear bands	Location of shear bands	Angle of shearing (α)	Depth of shear arc (d)
$R = 0$ (Kink)	1 triangular region	At kink	$\alpha = 36° \approx \theta + \alpha'$ $\alpha' \approx 10°$	No arc formed
$R = 2b = 5.2\ m$	2 triangular	At start and end of curve		Arc not visible due to small slope and curvature

3.3.3.3 Key findings regarding slope angle

On comparing the results from Tables 3.4 and 3.5, we can conclude that the slope angle does not have a big impact on the geometry of the internal shearing mechanism. Also, from the results, the magnitude of shearing consistently decreases with the reduction of θ.

3.3.4 Proposing a generalized internal shearing mechanism

Hence, given a landslide geometry with slope angle θ, radius of curvature R, friction coefficient μ ($\mu = tan\ \psi$), we **propose a generalized mechanism** for internal shearing of biplane compound landslides:

Kink transitions: Kink slope transitions will initially develop a vertical shear band at the kink, followed by a triangular shear band development. The edges of shear band are nearly perpendicular to the slope planes.

Curved transitions: The curved geometries with low radii would develop triangular shear bands with edges normal to basal slip planes. The shear arc will be small. Transitions with large radius of curvature would develop two distinct shear bands and a shear arc. The shear bands are located at the start and end of the curved transition, and the shear arc connects the two end points.

- The angle between adjacent edges of a triangular shear band (α) can be generally approximated by the slope angle θ, i.e. $\alpha \approx \theta$.
    - Due to forward movement of soil, the shear bands tend to increase by a small angle α'. For frictionless surfaces, the range of α' is 0 – 10°.
    - Due to the basal friction, the value of α may decrease. The change Δα is equal to the negative of the basal friction angle ψ, implying $\Delta\alpha \approx -\psi$.

      $$\alpha = \theta + \alpha' - \psi \qquad \text{(Equation 2)}$$

      The range of α' is 0 – 10°
- The shear arc extends from the start to end of the curvature. It becomes visible when the radius is more than half the maximum width of soil (b), i.e. R > 0.5*b.
    - The radius of the shear arc (d) is related to the analytical radius (r):

      $$d \approx k * r \qquad \text{(Equation 1)}$$

      where range of k: 1.0 – 1.3 ; and $r = R * tan\ (\theta/2)$

- The value of d is not influenced appreciably by the presence of friction.
- The shear mechanism observed in kink transitions can be considered a particular case of the curved transition.
- As θ increases, the magnitude of shearing also increases.

Please note that this is a preliminary study, and the effects of the material properties, landslide thickness, and surface topography were not accounted for.

3.4 Effects of internal shear mechanisms on the accumulated shear strain and material degradation

In the previous section, we determined the geometry of the internal shearing mechanism in biplanar compound landslides. We noted that the magnitude of internal shearing is more intense in landslides with kink slope transitions as compared to round geometries. Moving on, in this section, we qualitatively investigate the material degradation in terms of accumulated shear strain. First, we analyze the same slope angle $(\theta = 37°)$ considered earlier, and then, we examine another slope angle $(\theta = 30°)$ with a longer runout.

3.4.1 Material degradation for different slope transitions

The theoretical numerical model presented in Section 3.3.3 with a slope angle of $\theta = 37°$ is considered. For $b = 4$ m, five radii of curvature are analyzed, being $R = 0, b, 2b, 4b,$ and $6b$ (0 m, 4 m, 8 m, 16 m, and 24 m, respectively).

The cumulative deviatoric strain for these five models is examined to qualitatively evaluate the material degradation occurring at slope transition. Each simulation is run for 5 seconds. For all geometries, the time which the toe impacts the wall is approximately found to be in the range of 1.6 – 1.8 seconds after being set into motion; with the least time for the model having the largest curvature (Figure 3.20). At this moment, sufficient mass has passed the slope transition, and the toe of the landslide is about to impact the wall at the end of the model.

From Figure 3.20, it is seen that the mass above the slope transition does not have accumulated shear strain since the material in this zone moves together similar to a rigid

solid. Once the mass crosses through the shearing zones, the accumulated shear strain increases, and as soon as it reaches the horizontal basal surface, the shear strain remains essentially constant. The material that is initially located at the downside (near the toe) of the internal shearing mechanism, remains unsheared during the motion until it reaches the vertical wall at the end of the model. The shear strain accumulates along with a band, whose thickness (z) depends on the curvature of the transition zone. Note that for the kink case $(R=0)$, z is equivalent to the thickness of the landslide $(z = b)$. For curved transitions, as R increases, the degradation zone becomes thinner, leaving a band of unsheared material close to the basal sliding surface. This effect is the result of the development of the shear arc described in the previous sections.

It is important to note that for curved transitions if the runout of the landslide is small (less than the length of the internal failure mechanism) and the instability is a first-time failure, an unsheared zone with intact material can remain in between two degraded zones (Figure 3.20 d and e).

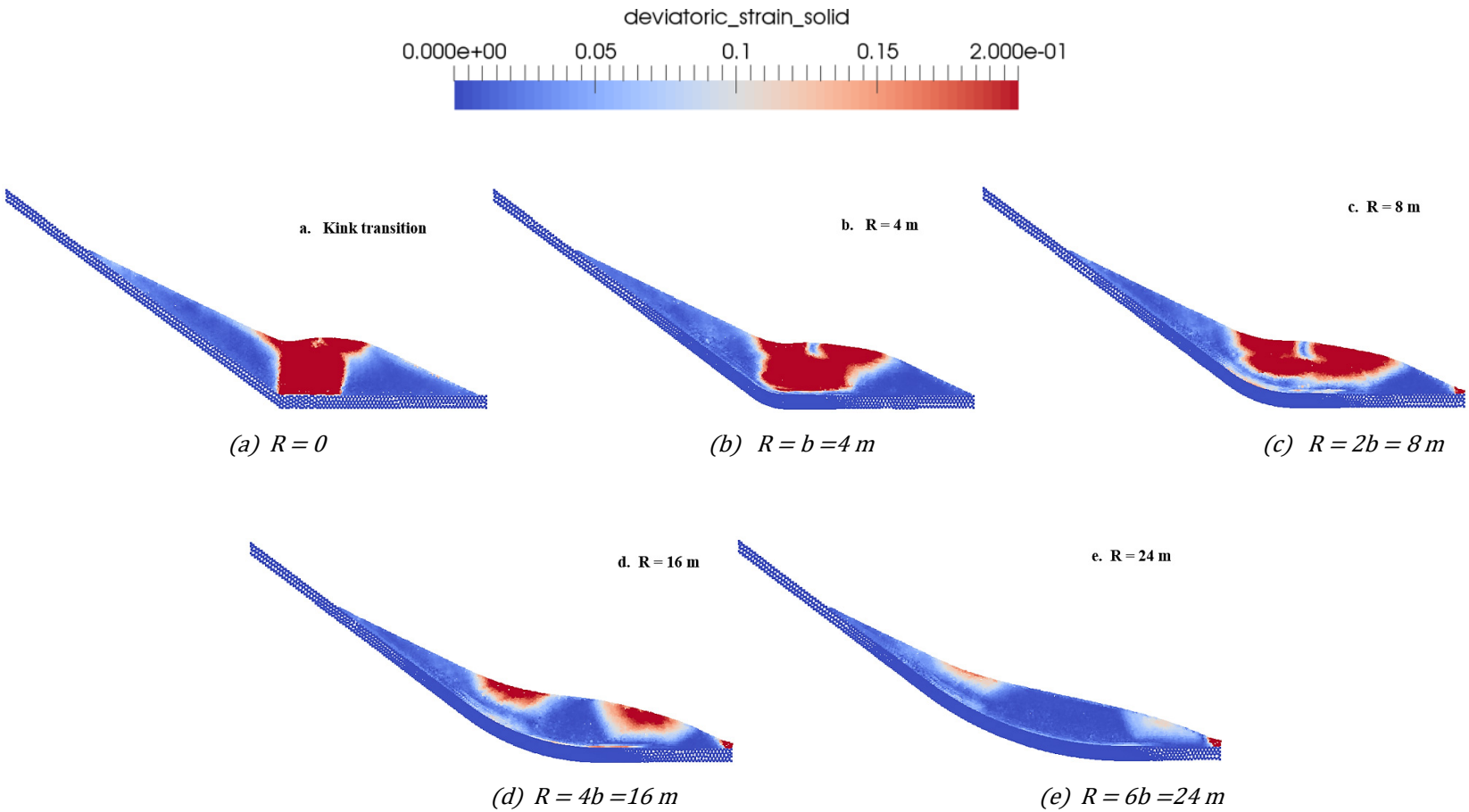

(a) R = 0 *(b) R = b =4 m* *(c) R = 2b = 8 m*

(d) R = 4b =16 m *(e) R = 6b =24 m*

Figure 3.20: Cumulative deviatoric strains for five landslide geometries just before impacting with wall

3.4.2 Effects of internal shear on material degradation for landslides with large runouts

In this section, the effects of internal shearing on the degradation of material in landslides with large runouts is discussed. A theoretical landslide geometry with slope angle $\theta = 30°$ is considered taking into account two slope transitions. Particularities of the model are $\theta = 30°, \beta = 30°, \mu = 0, h = 10.5\,m, x = 4\,m, b = 2\,m, X = 30\,m, H = 10.5\,m.$

Figure 3.21 represents the geometry with a kink slope transition. One variation of this geometry is a model with a curved transition of radius $R = 7.35*b = 14.7$ m. The slope instability is triggered using gravity and subsequently reducing the basal friction angle down to 0 ($\mu = 0$).

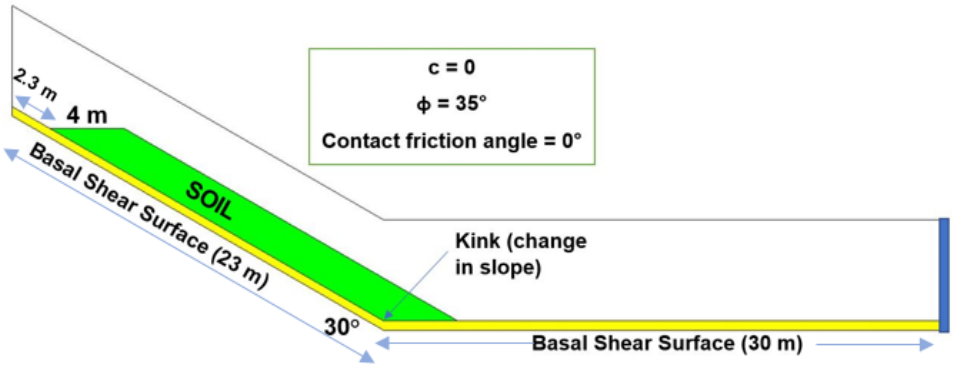

Figure 3.21: Kink slope transition geometry for slope angle, θ = 30°

First, the internal shearing mechanism proposed in section 3.3.4 is validated for this geometry. In Figure 3.22, the incremental deviatoric strain is visualized for kink and curved slope transitions.

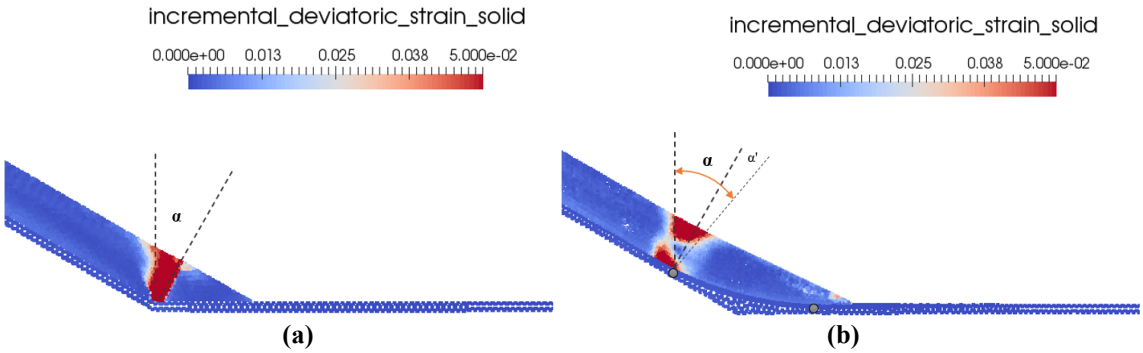

Figure 3.22: Internal shear pattern in kink and curved slope transitions (θ = 30°)

Intense shearing is observed at the kink slope transition, and a roughly triangular shear band originates from the kink and spreads to the soil surface. For the curved transition, strain localization occurs at the start of the curved transition. The shear angle $\alpha = 26 - 36°$, and is equal to the sum of slope angle θ and increment α', which agrees with our assumed failure mechanism hypothesis.

The cumulative deviatoric strain for the two models is presented at two times during the sliding process (t = 2 s and just before impacting the wall) in Figure 3.23. In Figure 3.23a, for the kink slope transition, a region of intense shear occurring as soon as soil crosses the internal shearing mechanism. For the curved transition case, the cumulative deviatoric strain is lesser, which implies the material is mostly unsheared, and therefore less degraded. Less energy losses occur, and the material mostly slides like a rigid body. Some shearing is observed at the top of the incline for both kink and curved geometries, which could be occurring due to difference in velocities of material points at the base and surface of the soil.

Figure 3.23b shows the accumulated deviatoric strain in both geometries just before impacting the wall at the end. A large red region is observed in kink slope case, which indicates intense shearing. For the round geometry, a large blue portion signifies less internal shearing and therefore, lower material degradation. On comparing the amount of shearing undergone in both cases, it can be said that material degradation occurring in slope transitions with high curvatures is less compared to sharp ones.

In this section, the material degradation of moving mass in a landslide was qualitatively visualized in terms of accumulated deviatoric strain. From our analysis, we can conclude that material in sharp/kink slope transitions undergoes more shearing and material degradation than curved/rounded geometries. Also, in large runouts, the material has already lost a significant portion of its energy due to internal shearing. Hence, internal shearing mechanism influences material degradation, which in turn leads to energy dissipation. In the next section, we will qualitatively study energy dissipation by analyzing impact forces of moving mass on a wall located at the end of horizontal basal surface.

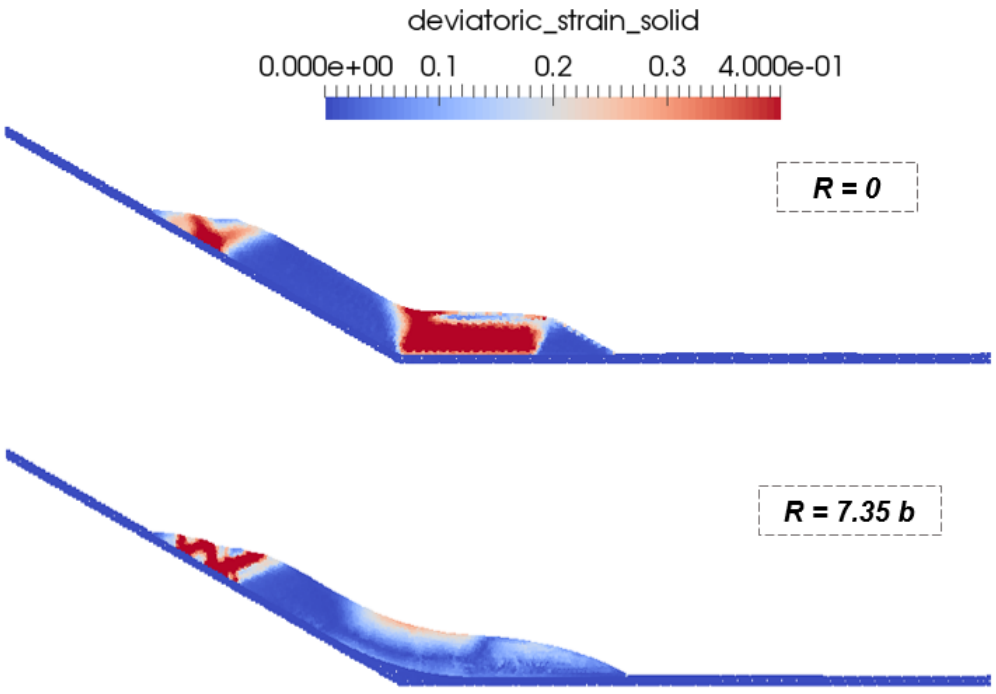

(a)

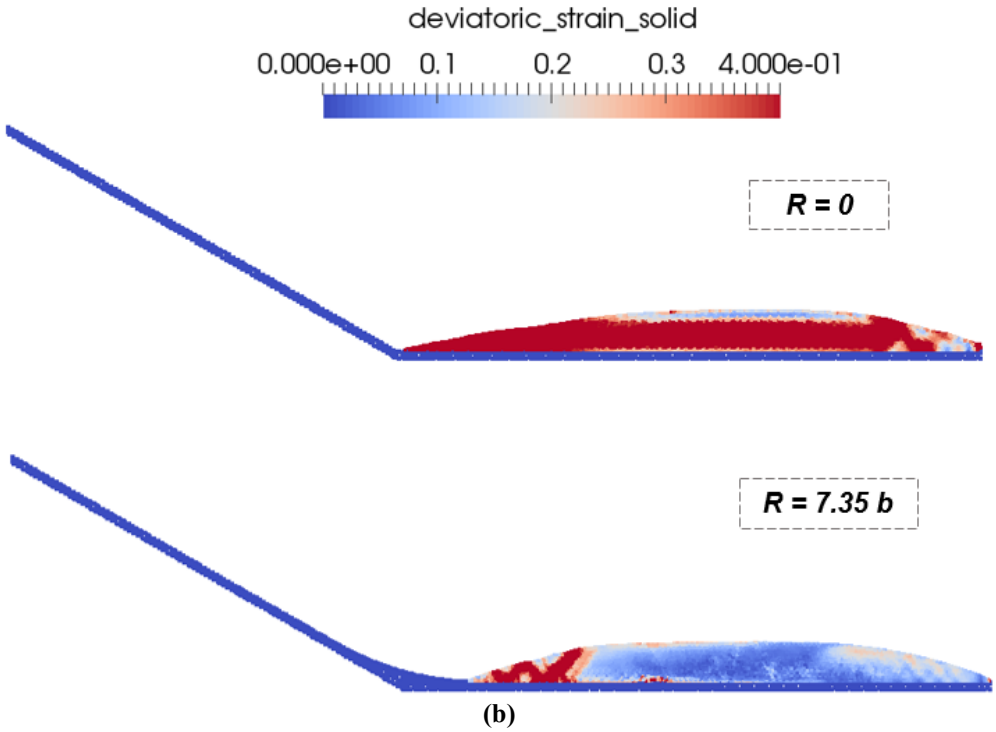

(b)

Figure 3.23: Cumulative deviatoric strain for kink and curved transition geometries at a) t = 2 s, and b) just before impacting wall.

3.5 Effect of internal shearing on energy dissipation in slope transitions

The capacity of damage caused by a landslide depends on the energy it possesses and on the amount of energy it is capable of transferring to a structure. Initially, a landslide possesses potential energy at rest due to its altitude. After a landslide is triggered, the material starts flowing down the slope, initiating the conversion of potential energy into kinetic energy, as per the law of energy conservation. At the lowest point of the slope, the energy possessed by the mass is mostly kinetic.

During the motion of soil, some energy is lost due to overcoming friction, plastic shearing, and interactions between grains. In particular, for compound landslides, one of the most relevant causes of energy loss is due to plastic internal shearing occurring along the basal surface and the internal shearing bands. Therefore, the amount of energy loss depends on the extent and type of internal shear formation patterns.

To qualitatively compute the energy loss due to different internal shearing mechanisms, the moving mass in the models is allowed to impact against a vertical rigid rough wall, and the reaction force as a result of the impact is measured. During the impact, the kinetic energy gets transferred to the wall before the landslide comes to rest. Therefore, analyzing the reaction forces on the wall as a result of the impact is an effective way to qualitatively estimate the energy dissipation taking place in different slope transitions.

We examine the impact forces on the wall for several slope transitions defined by radius of curvature. The impact forces are evaluated by calculating the total magnitude of the reaction force vector over a period of time.

3.5.1 Qualitative analysis of energy dissipation in terms of reaction forces for different slope transitions

In this section, we qualitatively estimate the effect of energy loss due to different slope transitions. The impact forces are determined on the vertical wall at the end the landslide model. First, the model presented in section 3.4.1 is considered for reference. Note that five different slope transitions are considered, and a small runout ($X = 3.75\,b$) is allowed. Figure 3.24 presents the evolution of the reaction forces on the wall with time.

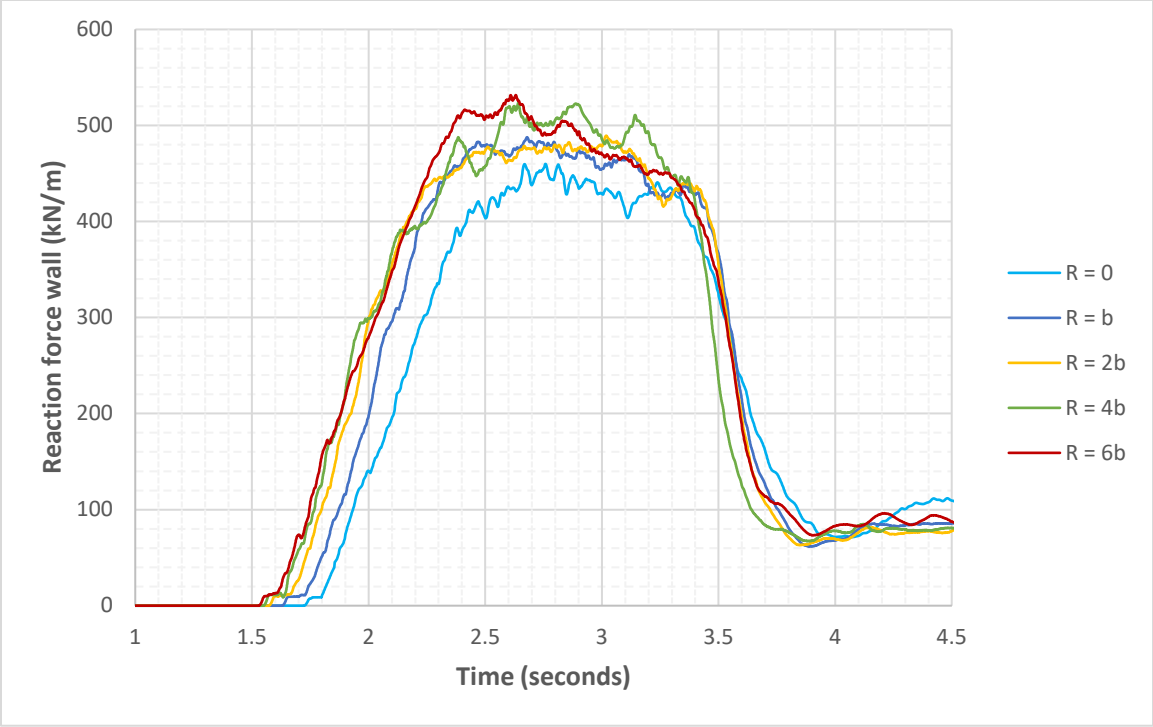

Figure 3.24: Combined plot of reaction forces exerted on wall by moving mass

Observations from Figure 3.24:

- $R = 0$ (Kink): The reaction force is lower than in curved geometries. The peak reaction force is as around 460 kN/m. The mobilized material impacts the wall latest of all cases, at nearly 1.7 seconds after the instability initiation, which indicates that the landslide velocity is the lowest.
- $R = b = 4\ m$: The average reaction force on the wall is more than the kink slope transition. The peak force is about 490 kN/m. This can be explained by the fact that particles undergo lower material degradation due to the presence of a curved transition instead of the sharp kink. The mass impacts the wall at about 1.65 seconds, which is also faster than the previous case.
- $R = 2b = 8\ m$: The average reaction force on the wall is more than that of R = 0 and R = 4 m case. The reaction peak is at about 495 kN/m. The time of impact is 1.6 seconds.

- $R = 4b = 16\ m$: The average reaction force on the wall is higher than in previous cases. The force peaks at about 520 kN/m at about 2.8 seconds. The moving mass impacts the wall at t = 1.55 seconds.
- $R = 6b = 24\ m$: The peak force magnitude is approximately 530 kN/m, which is the greatest of all the cases considered here. Due to a larger radius of curvature, the particles undergo less shearing, which means that the landslide possesses more kinetic energy at the moment of the impact hence a higher reaction force is required from the wall. The toe of the landslide reaches the wall the fastest, about 1.51 seconds after the landslide initiation.

Based on the results above, the reaction force exerted in the case of landslides with rounded geometries was generally greater than the ones with small curvatures (kink type transitions). This is because more internal shearing occurs in a kink slope transition, implying higher material degradation. So, more energy is dissipated at sharp slope changes (kink) which results in lower particle velocities as compared to particles in curved slope transitions.

3.5.2 Qualitative analysis of energy dissipation in terms of reaction forces for a longer runout

Here, we study the influence of roundedness on the energy dissipation phenomenon for a landslide with a longer runout ($X = 15\ b$). The geometry is the same as described in section 3.4.1. Again, the magnitude of the reaction force on the vertical wall is measured for two slope transitions ($R = 0, R = 7.35b$). The evolution of the reaction force is plotted in Figure 3.25. We observe the same pattern as for shorter runouts, but in this case, the differences in terms of average reaction force are even larger. Consistently, the rounded model reaches the wall faster than the model with a kink.

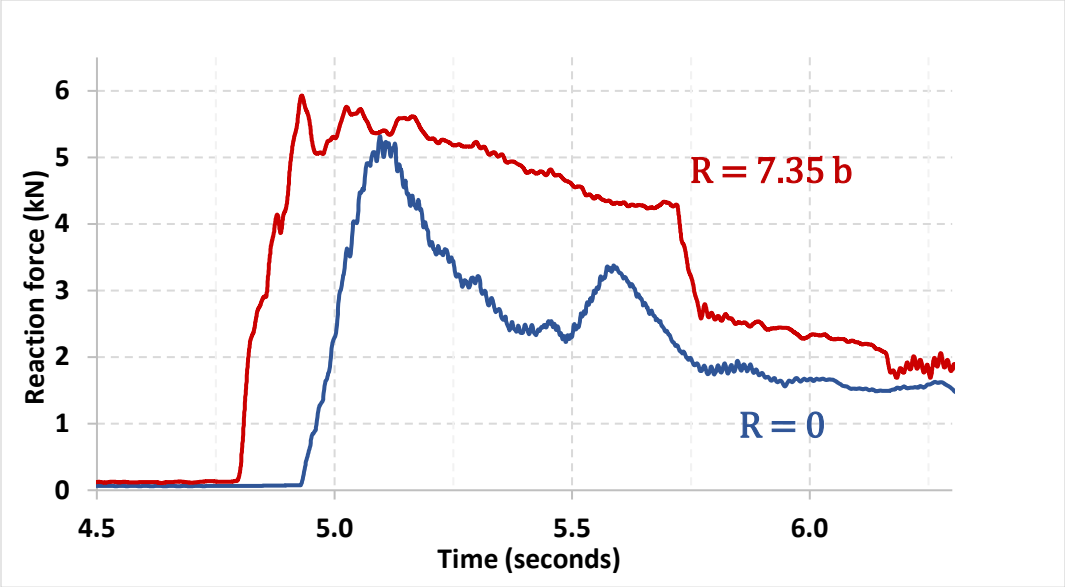

Figure 3.25: Evolution of reaction forces on the wall for kink and curved slope transitions

3.5.3 Key findings from reaction forces of the landslide on a vertical rigid wall:

- The capacity of damage caused by a landslide on a structure is related to the kinetic energy it possesses. This energy can be lost or dissipated during slope transitions and material degradation.
- More energy is dissipated in a kink slope transition which is qualitatively represented by lower reaction forces on the impact wall. The reaction force against the wall is larger for the rounded models than for the kink model. It is highest for the models with a larger radius and keeps on decreasing subsequently as the radius is decreased.
- In longer runouts, the influence of roundedness on energy dissipation is observed. A higher value of average impact force is estimated for large curvature landslide geometries. Lower reaction forces are found for kink slope transitions.
- Study of the energy dissipation in terms of reaction forces is an efficient and practical way of qualitatively investigating energy dissipation phenomena in compound landslides. This research can be extended to examine the impact of landslide on retaining structures.

3.6 Role of protective barriers in mitigating landslide damage (Preliminary insights)

To mitigate landslide damage, we examine the usefulness of protective barriers placed along the path of a landslide. The barriers are installed with an aim to slow down the moving mass and dissipate most of the kinetic energy of soil particles. In other words, we expect the barriers to reducing the velocity of moving mass of particles by bringing them to momentary stops at periodic intervals on the incline. This phenomenon enhances internal shearing and material degradation. Hence, the impact against further structures can be avoided or is minimized.

To analyze the numerical models for barrier efficiencies, a soil mass is placed at the top and which would slide down under the under the influence of gravity and hit the wall at the lower part of the incline. First, impact forces are calculated for a model with no barrier. Then, we simulate models with different number of barriers and spacings to note any changes in the impact forces. Finally, a comparison is drawn for impact forces on the wall for a different number of barriers and different spacings. Using impact forces as a practical method of visualization, we can qualitative estimate the energy losses occurring due to the involvement of protective barriers.

Kindly note that the results obtained in this section are very preliminary and simplistic intending to gain elementary insights on the role of barriers in landslide damage mitigation.

3.6.1 General numerical model

A new numerical model was developed to study the role of protective barriers. Figures 3.26 and 3.27 show numerical models with no barrier and 3 barriers, respectively. The geometry consists of a 26.5° slope followed by a vertical wall at the end to measure the impact force from the moving mass. The length of the basal shear surface is L and has a friction coefficient of 0.2. The distance between the soil block and the middle barrier is X. Barrier spacing and height are represented by c and h, respectively. Soil block has dimensions a by b. The mesh size used was 0.5 m, considering time optimization and result accuracy. Three material points per element are chosen for the soil and the plane. The soil material properties are consistent with Table 3.1.

The soil block is placed at the top of the slope and gravity is applied. The instability is triggered by a reduction from the basal friction coefficient, from fully rough to 0.2. Three sets of barriers with different height and spacing are considered– Type 1, Type 2, and Type 3 (Figure 3.28).

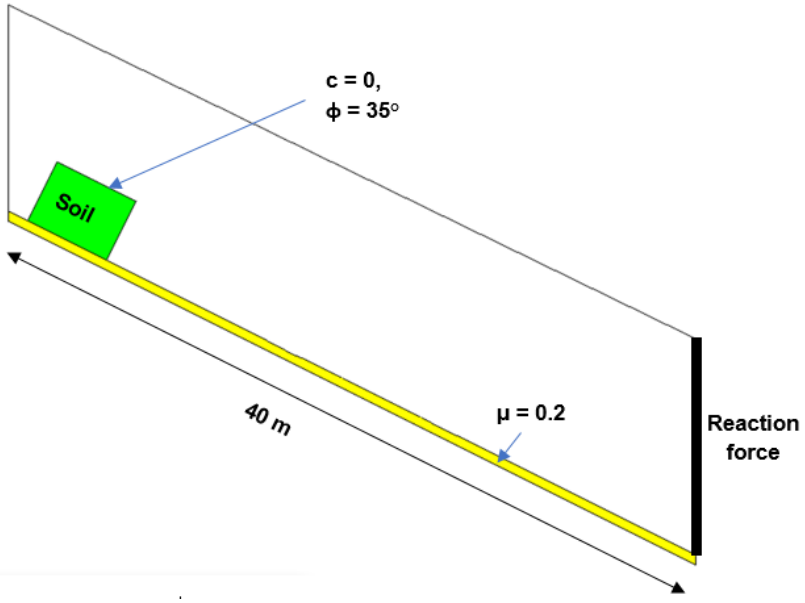

Figure 3.26: General numerical model with no barrier

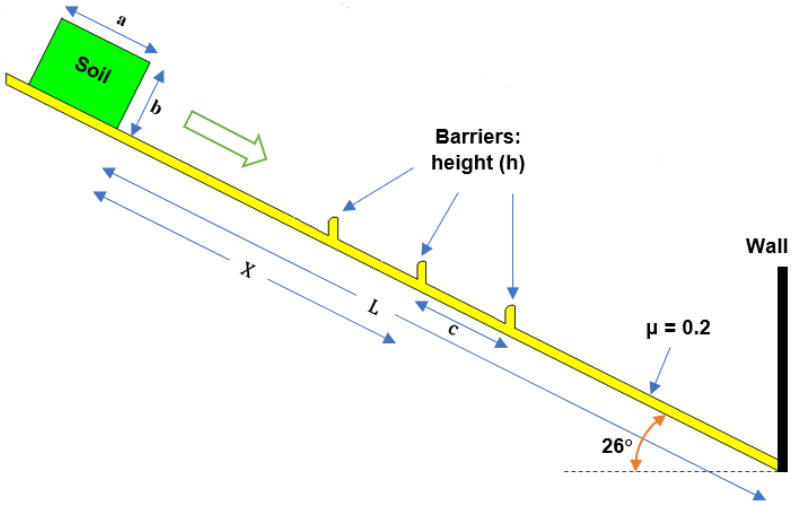

Figure 3.27: General numerical model with 3 barriers

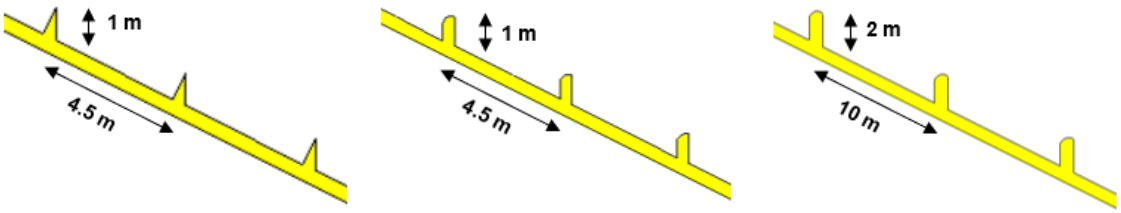

Type 1 Type 2 Type 3

Figure 3.28: Types of barriers used

3.6.2 Effect of using protective barriers

Protective barriers can be used to dissipate energy possessed by moving particles. These absorb the impact of motion, and reduce the momentum by bringing the particles to a momentary stop. We study energy dissipation in three types of barrier setup qualitatively by analyzing the loss in reaction forces on vertical wall.

3.6.2.1 Barriers Type 1

The Type-1 barriers have one edge vertical and one perpendicular to the incline. The spacing between the barriers is $c = 4.5\ m$ and barrier height, $h = 1\ m$. Other particularities: $X = 6.7\ m$, $L = 32\ m$. The soil block has dimensions: $a = 4.5\ m$ and $b = 3.4\ m$.

The simulations are run for 1 and 3 barriers, and are compared with the case of non-barriers. The reaction force on the end vertical wall is measured as a function of time for models with 0, 1, and 3 barriers. This force provides a qualitative estimate of the energy transferred in the impact. The plots in Figure 3.29 provides a graphical representation values of maximum impact forces vs number of barriers used.

From the results, the maximum reaction force on the wall is reduced by about 37.5% by just including one barrier on the incline located midway between the flowing soil and the wall. Furthermore, including three barriers would roughly reduce the force to half of the maximum force imparted on the wall with no barrier.

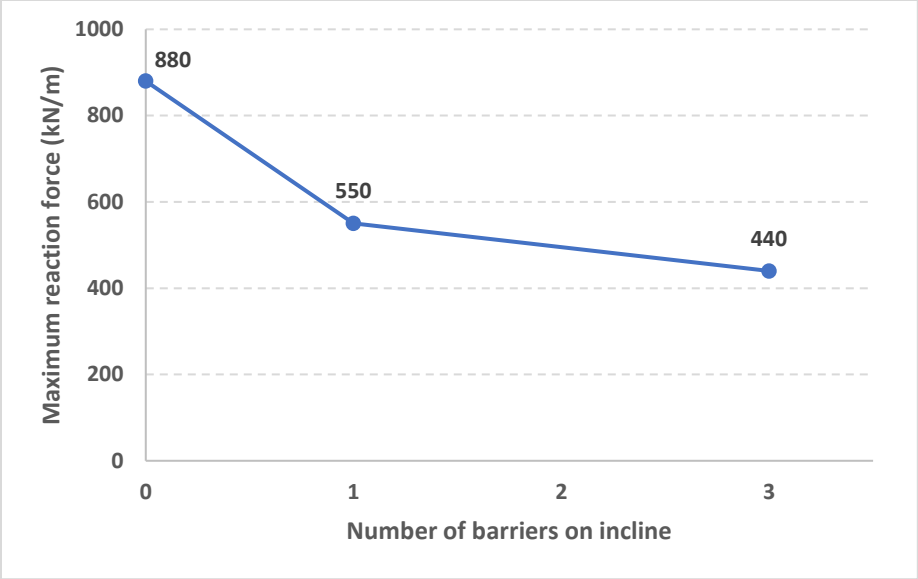

Figure 3.29: Impact forces on wall Vs number of barriers (Barriers Type-1)

Energy loss occurs on impact of soil with the barriers. Due to energy dissipated during the collision, the particles possess a lower kinetic energy, which means a lower moving velocity. So, at the final collision, the particles transfer less energy to the wall than they normally would have in the absence of protective barrier.

3.6.2.2 Barriers Type 2

Type 2 barriers are a slight variation to the shape of Type 1 barriers. In Type 2, the barrier edges are vertical and rounded at the top. All other model parameters remain same as described in section 3.6.1.1. The simulation is run for the 0, 1, 2 and 3 barriers. The plots in Figure 3.30 provides a graphical representation values of maximum impact forces vs number of barriers used. Similar trends for energy dissipation are reflected in Type 2 barriers also.

The reduction in reaction force is 52% for 1 barrier and about 70% for 3 barriers. It is noted that barriers rounded at the top are more effective in dissipating kinetic energy of moving mass.

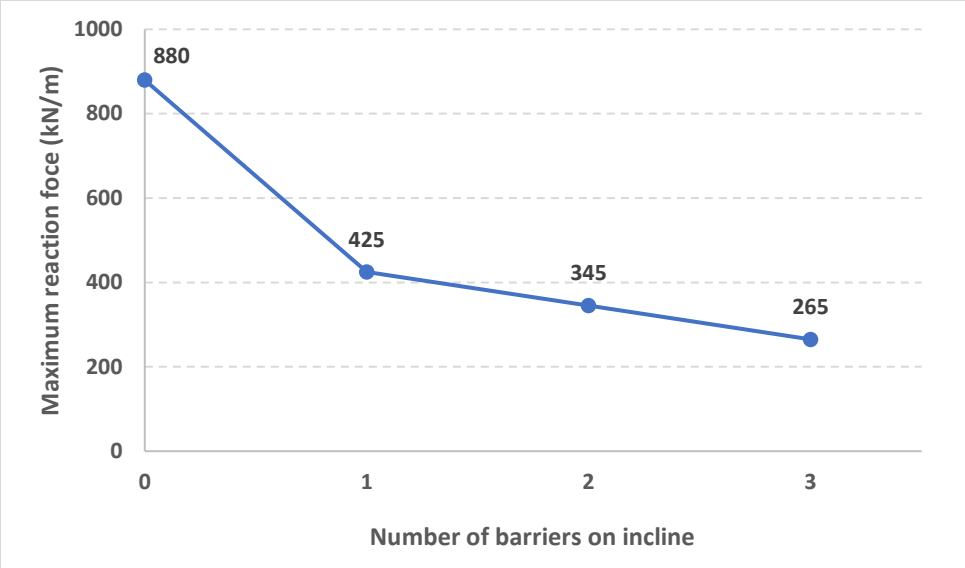

Figure 3.30: Impact forces on wall Vs number of barriers (Barriers Type-2)

3.6.2.3 Barriers Type 3

A larger numerical model is used in this simulation for simulating the response of Type-3 barriers. In this numerical model, length of slope is increased, and the soil block dimensions are changed. This is done to observe the any change in energy losses due to change in increased spacing between barriers. Particularities of the model: $c = 10\ m$, $h = 2\ m$, $X = 21\ m$, $L = 46\ m$. Soil dimensions: $a = 4.5\ m$, $b = 3.4\ m$.

Four numerical simulations are run: one each the model with 0, 1, 2, and 3 barriers. The reaction force on the wall is measured as a function of time for the 0, 1, 2, and 3 barrier cases. The plots in Figure 3.31 provides a graphical representation values of maximum impact forces vs number of barriers used.

It is noted that the maximum force is reduced by 26%, which is less than the reduction caused by closely spaced barriers used in Type 1 and Type 2. This may be due to a longer landslide runout, where, by virtue of gravity, the mass is able to regain the kinetic energy lost upon impact with a barrier. Also, for Type-3 barrier setup, the reduction is about 51%, which is less than Type-2 barrier orientation. This may be due to a larger barrier spacing in this setup as compared to the previous setup. It can be said that a greater number of barriers per unit length of runout would be more effective in reducing the final impact forces on a wall.

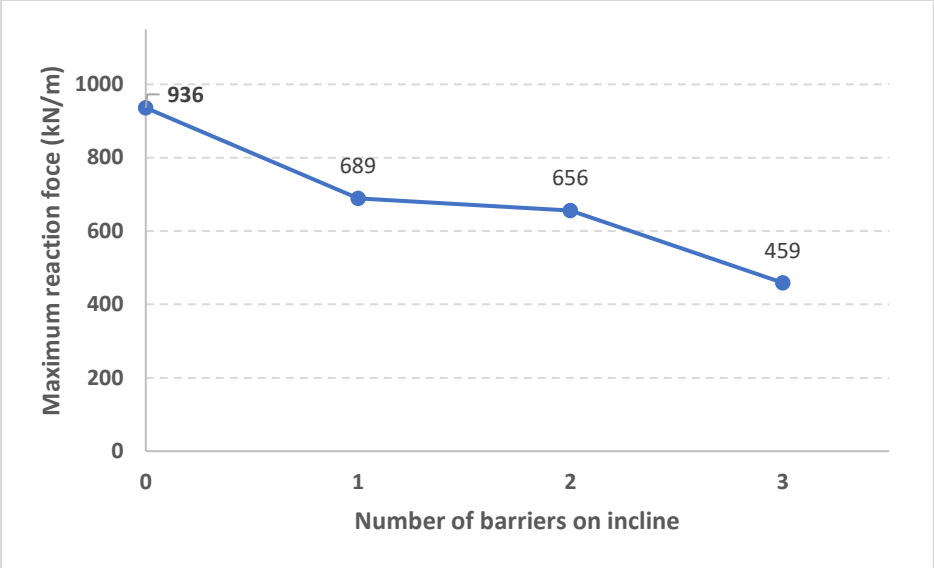

Figure 3.31: Impact forces on wall vs number of barriers (Barriers Type-3)

3.6.3 Key findings regarding protective barriers

From these simulations, we note that the maximum reaction force on the wall is roughly reduced by 25 – 50% by the introduction of just 1 barrier midway in the incline in the path of the moving mass (See Figure 3.32). Including 2 barriers reduces the maximum reaction by 30 – 60%. On using 3 barriers, the maximum reaction force on wall decreases by 50 – 70 %. These numbers suggest that using barriers are effective in dissipating a large amount of kinetic energy, and hence a useful technique to mitigate landslide damage.

The amount of soil mass that reaches the final structure (wall) decreases with increasing the number of barriers. During each collision, some soil momentarily stops, loses some of its momentum, and gets deposited at the barrier points. The effect is more pronounced if the spacing between the barriers is less, which makes more soil to get deposited at lower velocities (Figure 3.33). Hence, less soil mass, and less velocity at the destination means less momentum and less kinetic energy to encounter.

We conclude that a greater number of barriers with less spacing would be the most effective in mitigating damaging consequences of a landslide.

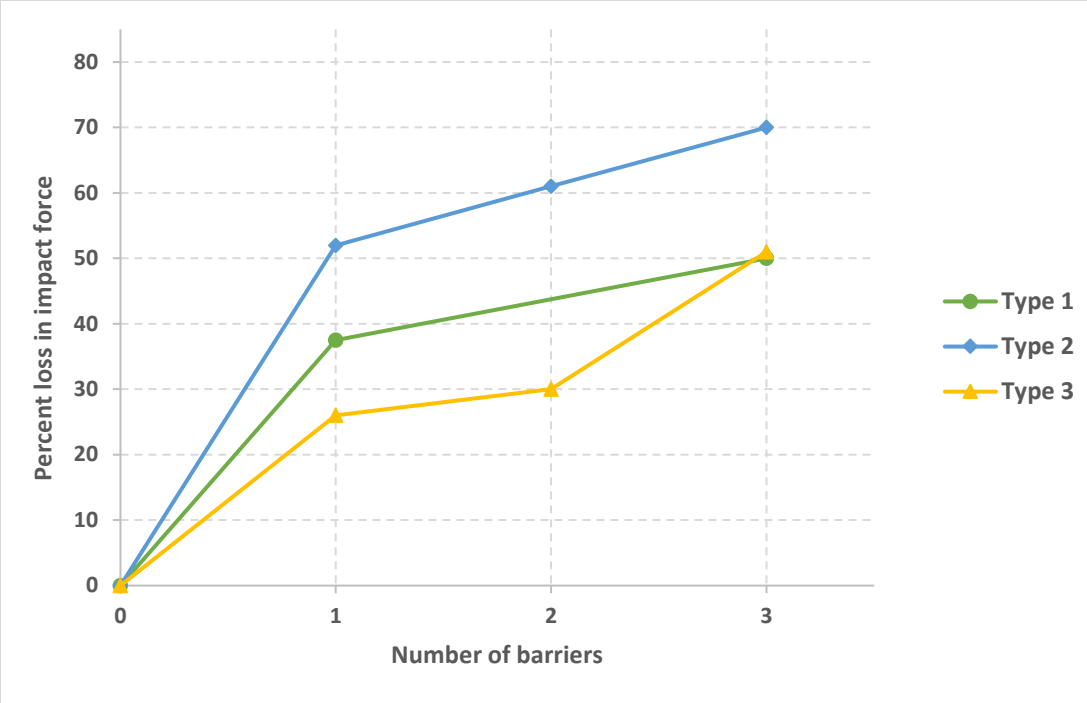

Figure 3.32: Percentage loss in impact forces for three types of barriers

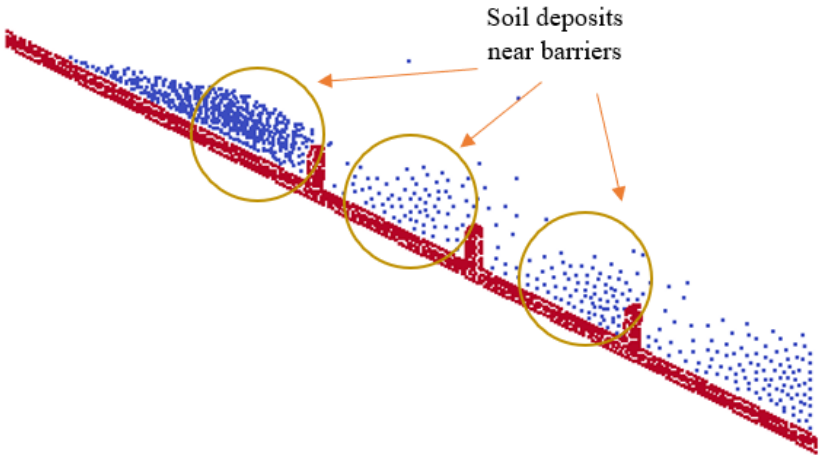

Figure 3.33: Soil deposits near barriers

4 Thesis Conclusions

4.1 Summary

The main objective of this thesis was to analyze the internal shearing mechanism in compound landslides and study some of their effects on landslide kinematics. First, the Material Point Method (MPM) was introduced, and the advantages and disadvantages were mentioned. After its validation, we first presented a general theoretical model of a landslide. Anura3D software and MPM were used to model the slope instabilities in compound biplanar landslides.

The study primarily focused on correlating internal shear patterns with the slope geometry. Models with a variety of slope transitions, slope angles (between 25 – 45°) and basal friction coefficients were simulated numerically to study the changes in failure mechanisms. A generalized failure mechanism was then proposed correlating the internal shear pattern with landslide geometry (R and θ).

This research also involved qualitatively studying material degradation and energy dissipation for different slope configurations as a result of the internal shearing. Impact forces measured on a wall at the end of the landslide runout was used to estimate kinetic energy losses. The cumulative deviatoric strain was assessed as a measure of material degradation.

The final part of this thesis aimed at gaining preliminary insights into the role of protective barriers in mitigating landslide damage. The number, spacing, and height of barriers were varied in different scenarios. We attempted to draw a relation between the characteristics of these barriers and the reduction in the reaction force on the final wall using different combinations of these parameters.

4.2 Key findings

Numerical models of compound landslides were developed and simulated using MPM algorithms for various types and geometries. Starting with a simplified approach is key to understand the basics of a problem followed by building complexity levels to produce

realistic results. After starting with simulating a simple model, the general mechanism of internal shearing was identified. High internal shearing occurs in a landslide at abrupt changes in slope, especially in a kink slope transition type of geometry, as compared to curved slope transitions.

A generalized failure mechanism is proposed based on numerical results that relates the failure geometry parameters *(α, d)* with the known landslide parameters *(R, θ, ψ).* Triangular regions with the sides perpendicular to the basal sliding surfaces constitute the boundaries of localized shear bands. In geometries with a large radius of curvature, these shear bands occur at the start and endpoint of the curved transition (Figure 4.1).

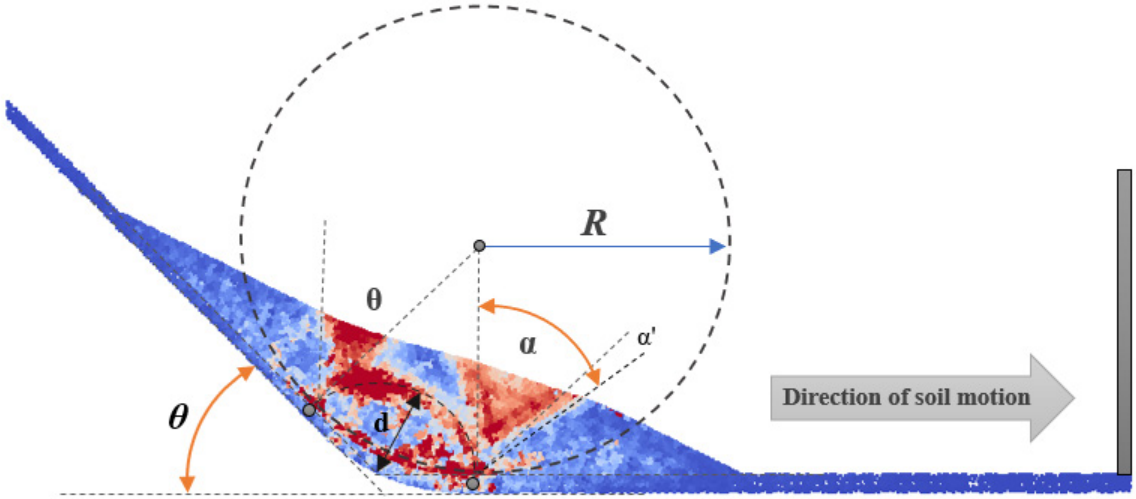

Figure 4.1: Schematic diagram depicting internal shear mechanism

α is the angle between the adjacent boundaries of shear bands with vertex at the point of slope change. Its value is approximately in the range of the slope angle *(θ)* of the landslide. α depends on the slope angle *(θ)* of landslide, increment *(α')*, and base friction angle (ψ) as $\alpha = \theta + \alpha' - \psi$, where α' lies between 0 - 10°. The triangular shear bands are connected by a curved shear band (shear arc). The radius of the shear arc *(d)* is closely related to the analytical radius (*r*) as $d = k * r$, where $r = \mathrm{R}\tan(\theta/2)$ and range of k is 1.0 – 1.3. Also, the value of *d* is not influenced appreciably by basal friction.

Energy dissipation and material degradation are qualitatively evaluated in this study. These are proportional to the degree to the cumulative deviatoric strain experienced after the development of a kinematically admissible mechanism in a compound landslide. More

energy was dissipated in the case of kink slope transitions, which renders the moving mass more sheared and degraded. Due to high energy losses experienced, the Material Points in a landslide with kink slope transition had a lower velocity than curved transition counterparts and would impact the wall latest among all the models. The corresponding impact forces on the wall are less, which translates to higher energy dissipation at the sharp changes on the slope.

The material degradation and energy dissipation due to sudden slope changes motivated us to investigate the use of barriers to mitigate landslide damage. The protective barriers along the landslide runout dissipate a portion of the kinetic energy of moving mass in a landslide. Closely spaced barriers with greater height and number proved to be most effective in mitigating damage. A reduction of about 25 - 50% was estimated in the case of 1 barrier, 30-60% on using 2 barriers and 50-70% on using 3 barriers installed on the landslide runout at regular intervals.

4.3 Recommendations for future work

Simple theoretical models of compound landslides are analyzed using MPM in this study. Although MPM can predict results for simple models with good accuracy, results might deviate when considering more complicated and realistic landslides involving complex topography, variable basal friction, variable material properties, and strength parameters along the slope. Physical experiments are therefore necessary to corroborate and validate the results obtained by numerical simulations in our analysis.

Also, all numerical models in this research assume Mohr-Coulomb constitutive model for soils to predict the internal shear mechanism in soils. This constitutive model has limitations and cannot be applied to all large-deformation problems. Further investigations may be required for better a calibration. Switching to more complex constitutive models that include grain-grain contacts would be vital to predicting post-failure behavior of compound landslides with higher levels of accuracy.

Most of the numerical models developed in this study are 2D plain strain models which might not fully capture the real-world behavior of complex materials like soils and rocks.

Developing full-scale 3D models of landslides would be a good idea to replicate real world scenarios of landslide that already occurred and calibrate those to predict post-failure behavior of landslides in disaster-prone area. However, developing 3D models also comes at a very high computation cost which might not be feasible in all situations. One needs to find a balance between the accuracy and cost of calculated results which would depend on the scale, scope, and importance of the problem in question.

The energy dissipation was qualitatively estimated by means of impact forces on the wall and material degradation using analyzing accumulated strain. A quantitative method of predicting the exact energy dissipation is necessary to obtain numerical values that are directly applicable for design purposes, such as retaining structures.

Further, very elementary results were obtained for the role of protective barriers in landslide damage mitigation. Better numerical models and efficient barrier designs are required to improve upon the basic models used in this research and develop sound mitigation techniques helpful in countering landslide damage.

Bibliography

Alonso, E. E., Pinyol, N. M., and Yerro, A. (2014). "Mathematical Modelling of Slopes." *Procedia Earth and Planetary Science*, 9, 64–73.

Brackbill, J. U., and Ruppel, H. M. (1986). "FLIP: A method for adaptively zoned, particle-in-cell calculations of fluid flows in two dimensions." *Journal of Computational Physics*, 65(2), 314–343.

Courant, R. (1943). "Variational methods for the solution of problems of equilibrium and vibrations." *Bulletin of the American Mathematical Society*, 49(1), 1–24.

Cuomo, S., Moretti, S., and Aversa, S. (2019). "Effects of artificial barriers on the propagation of debris avalanches." *Landslides*, 16(6), 1077–1087.

Fell, R., Glastonbury, J., and Hunter, G. (2007). "Rapid landslides: the importance of understanding mechanisms and rupture surface mechanics." *Quarterly Journal of Engineering Geology and Hydrogeology*, 40(1), 9–27.

Fern, J., Rohe, A., Soga, K., and Alonso, E. (Eds.). (2019). *The Material Point Method for Geotechnical Engineering*. CRC Press, Boca Raton : CRC Press, Taylor & Francis Group, [2019].

Gingold, R. A., and Monaghan, J. J. (1977). "Smoothed particle hydrodynamics: theory and application to non-spherical stars." *Monthly Notices of the Royal Astronomical Society*, 181(3), 375–389.

Glastonbury, J., and Fell, R. (2010). "Geotechnical characteristics of large rapid rock slides." *Canadian Geotechnical Journal*, 47(1), 116–132.

Harlow, F. H. (1962). *The particle-in-cell method for numerical solution of problems in fluid dynamics*. Los Alamos, NM (United States).

"How many deaths result from landslides each year?" (n.d.). <https://www.usgs.gov/faqs/how-many-deaths-result-landslides-each-year?qt-news_science_products=0#qt-news_science_products> (May 29, 2020).

Hungr, O., Leroueil, S., and Picarelli, L. (2014). “The Varnes classification of landslide types, an update.” *Landslides*, 11(2), 167–194.

Hutchinson, J. N. (1987). “Mechanisms producing large displacements in landslides on pre-existing shears.” *Memoir of the Geotechnical Society of China*, 9, 175–200.

Idelsohn, S. R., Oñate, E., Pin, F. Del, and Calvo, N. (2006). “Fluid–structure interaction using the particle finite element method.” *Computer Methods in Applied Mechanics and Engineering*, 195(17–18), 2100–2123.

Li, B., Habbal, F., and Ortiz, M. (2010). “Optimal transportation meshfree approximation schemes for fluid and plastic flows.” *International Journal for Numerical Methods in Engineering*, 83(12), 1541–1579.

Liszka, T., and Orkisz, J. (1980). “The finite difference method at arbitrary irregular grids and its application in applied mechanics.” *Computers & Structures*, 11(1–2), 83–95.

Mancarella, D., and Hungr, O. (2010). “Analysis of run-up of granular avalanches against steep, adverse slopes and protective barriers.” *Canadian Geotechnical Journal*, 47(8), 827–841.

Ng, C. W. W., Choi, C. E., Koo, R. C. H., Goodwin, G. R., Song, D., and Kwan, J. S. H. (2018). “Dry granular flow interaction with dual-barrier systems.” *Géotechnique*, 68(5), 386–399.

Petley, D. (2012). “Global patterns of loss of life from landslides.” *Geology*, 40(10), 927–930.

Sabel, M., Sator, C., and Müller, R. (2014). “A particle finite element method for machining simulations.” *Computational Mechanics*, 54(1), 123–131.

Soga, K., Alonso, E., Yerro, A., Kumar, K., Bandara, S., Kwan, J. S. H., Koo, R. C. H., Law, R. P. H., Yiu, J., Sze, E. H. Y., and Ho, K. K. S. (2018). “Trends in large-deformation analysis of landslide mass movements with particular emphasis on the material point method.” *Géotechnique*, 68(5), 457–458.

Sulsky, D., Chen, Z., and Schreyer, H. L. (1994). “A particle method for history-dependent

materials." *Computer Methods in Applied Mechanics and Engineering*, 118(1–2), 179–196.

Sulsky, D., and Schreyer, H. L. (1996). "Axisymmetric form of the material point method with applications to upsetting and Taylor impact problems." *Computer Methods in Applied Mechanics and Engineering*, 139(1–4), 409–429.

Yerro, A., Alonso, E. E., and Pinyol, N. M. (2016a). "Run-out of landslides in brittle soils." *Computers and Geotechnics*, 80, 427–439.

Yerro, A., Pinyol, N. M., and Alonso, E. E. (2016b). "Internal Progressive Failure in Deep-Seated Landslides." *Rock Mechanics and Rock Engineering*, 49(6), 2317–2332.